The Astrophysical Journal, 969:97 (17pp), 2024 July 10 https://doi.org/10.3847/1538-4357/ad46d9

A Panchromatic Study of the X-Ray Binary Population in NGC 300 on Subgalactic Scales

Breanna A. Binder[1], Rosalie Williams[1], Jacob Payne[1], Michael Eracleous[2], Alexander Belles[2], and Benjamin F. Williams[3]
[1] Department of Physics & Astronomy, California State Polytechnic University, 3801 W. Temple Ave, Pomona, CA 91768, USA; babinder@cpp.edu
[2] Department of Astronomy & Astrophysics and Institute for Gravitation and the Cosmos, The Pennsylvania State University, 525 Davey Lab, University Park, PA 16802, USA
[3] Department of Astronomy, University of Washington, Box 351580, Seattle, WA 98195, USA
Received 2023 October 19; revised 2024 April 16; accepted 2024 April 26; published 2024 July 10

Abstract

The population-wide properties and demographics of extragalactic X-ray binaries (XRBs) correlate with the star formation rates (SFRs), stellar masses ($M_\star$), and environmental factors (such as metallicity, Z) of their host galaxy. Although there is evidence that XRB scaling relations (L_X/SFR for high-mass XRBs (HMXBs) and $L_X/M_\star$ for low-mass XRBs) may depend on metallicity and stellar age across large samples of XRB-hosting galaxies, disentangling the effects of metallicity and stellar age from stochastic effects, particularly on subgalactic scales, remains a challenge. We use archival X-ray through IR observations of the nearby galaxy NGC 300 to self-consistently model the broadband spectral energy distribution and examine radial trends in its XRB population. We measure a current (<100 Myr) SFR of 0.18 ± 0.08 $M_\odot$ yr^{-1} and stellar mass $M_\star = (2.15^{+0.26}_{-0.14}) \times 10^9$ $M_\odot$. Although we measure a metallicity gradient and radially resolved star formation histories that are consistent with the literature, there is a clear excess in the number of X-ray sources below $\sim 10^{37}$ erg s^{-1} that are likely a mix of variable XRBs and additional background active galactic nuclei. When we compare the subgalactic L_X/SFR ratios as a function of Z to the galaxy-integrated L_X-SFR-Z relationships from the literature, we find that only the regions hosting the youngest ($\lesssim$30 Myr) HMXBs agree with predictions, hinting at time evolution of the L_X–SFR–Z relationship.

Unified Astronomy Thesaurus concepts: X-ray binary stars (1811); High mass x-ray binary stars (733); Compact objects (288); Spiral galaxies (1560)

Supporting material: machine-readable tables

1. Introduction

Some of the most useful laboratories for studying binary star evolution are X-ray binaries (XRBs), which contain a compact object (either a neutron star (NS) or a black hole (BH)) accreting mass from a stellar companion. High-mass XRBs (HMXBs) contain a massive ($\geqslant$8 $M_\odot$) and often post-main-sequence companion and represent a critical phase in the history of massive star evolution: their current properties are the result of the orbital and mass-exchange history of the progenitor binary, and the ultimate fate of some of these binaries is to form millisecond pulsars, short gamma-ray bursts, or double compact object systems capable of generating detectable gravitational wave signals. Feedback from HMXBs is now recognized as an important contributor to heating the intergalactic medium and reionizing the early Universe (Kaur et al. 2022).

It is now well established that the X-ray luminosity functions (XLFs) and population-integrated luminosities (L_X) of HMXBs scale with host galaxy star formation rate (SFR; Grimm et al. 2003; Ranalli et al. 2003; Gilfanov et al. 2004; Mineo et al. 2012), while those of low-mass XRBs (LMXBs, which typically contain companions of $\sim$1–2 $M_\odot$) track host galaxy stellar mass ($M_\star$; Colbert et al. 2004; Gilfanov 2004; Lehmer et al. 2010; Boroson et al. 2011; Zhang et al. 2012). Previous studies have attempted to empirically measure the dependence of XRB scaling relations ($L_X^{\rm HMXB}$/SFR or $L_X^{\rm LMXB}/M_\star$) on physical parameters such as age (Kim & Fabbiano 2010; Lehmer et al. 2014) and metallicity (Basu-Zych et al. 2013; Douna et al. 2015; Basu-Zych et al. 2016; Brorby et al. 2016; Tzanavaris et al. 2016). Population synthesis models predict that the these scaling relations in XRB populations can vary by up to an order of magnitude depending on the metallicity and age of the XRB population (Fragos et al. 2008; Linden et al. 2010; Fragos et al. 2013a, 2013b; Zuo et al. 2014). Nearby galaxies, where XRB populations can be spatially resolved with X-ray telescopes such as Chandra and XMM-Newton, span a relatively narrow range in metallicities while hosting a larger diversity of stellar ages when compared to distant galaxies, and have experienced a wide variety of star formation histories (SFHs) and merger/interaction histories. As such, we do not yet precisely understand how the XRB scaling relations vary with SFH and metallicity.

Studies of the HMXB L_X/SFR fraction as a function of metallicity (hereafter referred to as the L_X–SFR–Z relation; e.g., Brorby et al. 2014; Basu-Zych et al. 2016) have largely concentrated on high-$M_\star$ galaxies with high SFRs where the XRB populations are expected to be dominated by HMXBs, and the XLFs are well sampled. However, these studies implicitly assume that the *global* average SFR and metallicity of galaxies adequately reflect the subkiloparsec scale environments in which HMXBs form. Due to their short lifetimes, HMXBs do not migrate more than a few hundred parsecs from their birthplaces (Bodaghee et al. 2012; Binder et al. 2023), and these temporal and spatial scales are shorter than those over which chemical mixing efficiently occurs in galaxies (Kreckel et al. 2020). Local variations in stellar populations and the HMXBs associated with them thus become "smeared out" on

Table 1
Basic Properties of NGC 300

Distance[a] (Mpc) (1)	R.A. (J2000) (2)	Decl. (J2000) (3)	$N_{H,Gal}$[b] (cm^{-2}) (4)	A_V[c] (mag) (5)	$E(B-V)$[c] (mag) (6)	Position Angle[d] (deg) (7)	Inclination Angle[d] (deg) (8)
2.0	00:54:53.48	−37:41:03.8	10^{21}	0.035	0.011	111	45

References.
[a] Dalcanton et al. (2009).
[b] HI4PI Collaboration et al. (2016).
[c] Schlafly & Finkbeiner (2011).
[d] de Vaucouleurs et al. (1991).

galaxy-wide scales, and may complicate interpretations of the L_X/SFR scaling relation (Kouroumpatzakis et al. 2020). Optical integral field units now make it possible to study thousands of subkiloparsec scale regions across the star-forming disks of nearby galaxies, and 2D metallicity maps demonstrate that metallicity variations occur on small scales (Williams et al. 2022), and many nearby galaxies exhibit metallicity gradients (see, e.g., Belfiore et al. 2019, and references therein).

The nearby (2.0 Mpc, based on measurements of the tip of the red giant branch; Dalcanton et al. 2009) star-forming galaxy NGC 300 is a particularly suitable target for studying XRBs in subgalactic environments. Numerous X-ray point sources are detected within the star-forming disk, which can be imaged in a single Chandra pointing down to limiting luminosities on the order of $\sim 10^{36}$ erg s^{-1} (Binder et al. 2012, 2017). The galaxy has been observed across nearly the entire electromagnetic spectrum, and exhibits a metallicity gradient with metallicity decreasing by $\sim 0.08 Z_\odot$ kpc^{-1} (Gogarten et al 2010; Kudritzki et al. 2008). The SFR of NGC 300 is generally reported to be $\sim 0.08 - 0.46\ M_\odot\ yr^{-1}$ by different tracers, such as the Hubble Space Telescope (HST) resolved stellar populations (Gogarten et al. 2010), UV observations (Mondal et al. 2019), Hα emission (Karachentsev & Kaisina 2013), and mid-IR observations (Helou et al. 2004). NGC 300 contains an ultraluminous X-ray source (ULX; e.g., see review by Binder et al. 2020 and references therein) and the luminous Wolf–Rayet + BH binary NGC 300 X-1 (Binder et al. 2021), although the majority of XRBs in the galaxy are of lower luminosity ($\sim 10^{36-37}$ erg s^{-1}; Binder et al. 2012, 2017), and the specific SFR of NGC 300 suggests that its XRB population is likely a mix of HMXBs and LMXBs (Lehmer et al. 2019).

We use archival multiwavelength observations to self-consistently model the stellar mass ($M_\star$), SFH, metallicity, and XRB population of NGC 300 on subgalactic scales and search for trends in the L_X/SFR ratio for HMXBs as a function of metallicity and stellar age. The paper is organized as follows: in Section 2, we summarize the archival far-UV (FUV)-IR observations used and our methodology for performing aperture photometry, and present spectral energy distributions (SEDs) for NGC 300. We additionally describe how the SED modeling package PROSPECTOR (Leja et al. 2017) is used to extract SFHs, stellar masses, and metallicities for the subgalactic regions within NGC 300. In Section 3, we describe the Chandra X-ray observations and compare the observed X-ray point-source population to predicted populations based on prior studies of the XLFs of HMXBs, LMXBs, and the active galactic nucleus (AGN) log$N$-log$S$ distribution. We discuss our results in Section 4, and conclude with a summary of our main findings in Section 5. All uncertainties correspond to the 90% confidence interval unless otherwise specified. Table 1 summarizes the main properties of NGC 300 that we assume throughout this work, including the distance, central R. A. and decl. coordinates, Galactic absorbing column, A_V, and position and inclination angles. The distance to NGC 300 was measured directly by Dalcanton et al. (2009) using the tip of the red giant branch, and is thus independent of cosmology.

2. Spectral Energy Distributions

2.1. The Data

In this section, we summarize the publicly available multiwavelength observations used to build the SEDs of NGC 300. Foreground stars were identified using the Gaia DR3 catalog (Gaia Collaboration et al. 2023) and through visual inspection of multiwavelength images and then masked with circular apertures with radii of $\sim 15''$. The median flux density per unit area of the corresponding subgalactic region in which each star was located was used to approximate the flux density of the galaxy in the masked region.

We note that, although NGC 300 has been imaged many times with the HST, the archival HST observations do not optimally cover the star-forming disk of NGC 300 and were obtained for a variety of filter configurations. For example, HST/F606W imaging covers only ∼50% of the star-forming disk of NGC 300, while F475W imaging covers less than ∼20% of the disk. Inferring galaxy-integrated optical flux densities from HST would require a significant degree of extrapolation and carry significant uncertainty, limiting their utility for SED modeling. We therefore do not include these data in our SED modeling.

2.1.1. Spitzer IRAC and MIPS

We first retrieved Spitzer IRAC and MIPS mosaics from the NASA/IPAC Infrared Science Archive (IRSA).[4] The IRAC channels have central wavelengths of 3.6, 4.5, 5.8, and 8.0 μm, while the MIPS channels have central wavelengths of 24, 70, and 160 μm. The IRAC images have an angular resolution $\sim 2''$, while the angular resolution of the MIPS images are $\sim 6''$, $\sim 18''$, and $\sim 40''$ at 24, 70, and 160 μm, respectively (Rieke et al. 2004). All Spitzer images have units of MJy sr^{-1}.

We measured the surface brightness profile of NGC 300 using the IRAC1 (3.6μm) image. We constructed a set of 25 elliptical annuli centered on the galaxy center and using a position angle of 111° for the major axis. The resulting surface

[4] https://irsa.ipac.caltech.edu/data/SPITZER/Enhanced/SEIP/overview.html

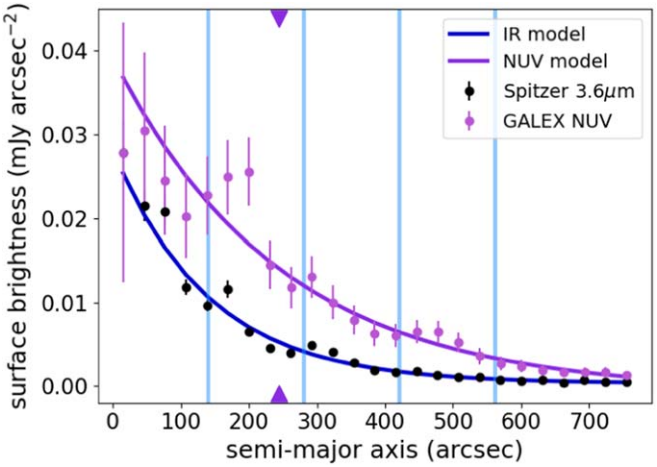

Figure 1. The Spitzer/IRAC 3.6 μm surface brightness profile (in mJy arcsec^{-2}; data in black; best-fit exponential disk model in blue) of NGC 300, with the four radial bins (each with a width of R_d=1.36 kpc) indicated by vertical light blue lines. The GALEX NUV surface brightness (normalized to the peak value of the 3.6 μm profile) is shown in purple. The purple upward and downward triangle indicates the scale length of the NUV disk.

brightness profile, in units of mJy arcsec^{-2}, is shown by the black dots in Figure 1. We modeled the surface brightness profile with an fit an exponentially decaying function,

$$I(r) = I_0 e^{-r/R_d} + I_{\rm bkg}, \quad (1)$$

using SciPy's `curve_fit` package, where I_0 is the central surface brightness, R_d is the disk scale length, and $I_{\rm bkg}$ is the background level surface brightness. We find best-fit parameters $I_0 = (2.79 \pm 0.14) \times 10^{-5}$ Jy arcsec^{-2}, $R_d = (140.3 \pm 4.7)$ arcsec (corresponding to a physical length of 1.36 ± 0.05 kpc), and $I_{\rm bkg} = (3.20 \pm 0.47) \times 10^{-7}$ Jy arcsec^{-2} (see the blue line in Figure 1). This scale length is consistent with those measured in previous optical and IR studies (Gogarten et al. 2010; Jang et al. 2020). The UV disk of NGC 300 is known to be more extended than the optical/IR disk ($\sim$2.7 kpc in the near-UV, hereafter NUV, see Mondal et al. 2019). For comparison, we also show the Galaxy Evolution Explorer (GALEX) NUV surface brightness profile in Figure 1, for which we measure a scale length of $\sim$2.4 kpc (see Section 2.1.5 for a discussion of GALEX data.)

The 3.6 μm scale length was then used to divide the galaxy into four equal-width radial bins. We opted for the 3.6 μm scale length, rather than the more extended NUV scale length for three main reasons: (1) the smaller annular regions reduce the amount of "smearing out" of key environmental factors such at metallicity and SFH, both of which are known to vary across the NGC 300 disk (Kudritzki et al. 2008; Gogarten et al. 2010); (2) since the expected AGN contribution increases with surface area, utilizing smaller annular regions reduces the expected contribution from AGN within each ring; and (3) at many wavelengths, the relative uncertainty in the fainter flux densities at large galactocentric radius results in more uncertain SED models (see Section 2). The four radial bins are an "inner" bin ($r \leqslant R_d$), an "inner middle" bin ($R_d < r \leqslant 2R_d$), an "outer middle" bin ($2R_d < r \leqslant 3R_d$), and an "outer" bin ($3R_d < r \leqslant 4R_d$). At a distance of 4R$_{\rm d}$, the surface brightness falls to $e^{-4} \approx 1.8\%$ of the central value; the uncertainties in the total flux density beyond 4R$_{\rm d}$ are large, diminishing our ability to confidently constrain the metallicity, stellar mass, and SFR in these outer regions.

2.1.2. WISE

We used the Wide-field Infrared Survey Explorer (WISE) Image Service hosted on the NASA/IPAC IRSA[5] to retrieve WISE images in bands W1 (3.4 μm), W2 (4.6 μm), W3 (12 μm), and W4 (22μm). The angular resolution is 6.″1, 6.″4, 6.″5 and 12″ for the W1, W2, W3, and W4 bands, respectively (Wright et al. 2010). Instrumental magnitudes are converted to AB magnitudes using the magnitude zero-points for each filter (in order of increasing central wavelength, 20.5, 19.5, 18.0, and 13.0 mag) and the AB magnitude offset defined for each band (in order of increasing central wavelength, 2.70, 3.34, 5.17, 6.62 mag; Cutri et al. 2013).

2.1.3. 2MASS

We retrieved background-subtracted FITS images of NGC 300 from the Two Micron All Sky Survey (2MASS) Large Galaxy Atlas[6] (Jarrett et al. 2003). The J, H, and K_s bands used by 2MASS are particularly sensitive to older stellar populations, which dominate the stellar mass of NGC 300 (Gogarten et al. 2010). The 2MASS images have an angular resolution of $\sim$4″, and the photometric zero-point calibration of the images is accurate to $\sim 2\% - 3\%$.

2.1.4. Swift Ultraviolet/Optical Telescope

We retrieved all available data from the Ultraviolet/Optical Telescope on the Neil Gehrels Swift Observatory from the High Energy Astrophysics Science Archive Research Center[7] that are within 17 arcmin of NGC 300 (Gehrels et al. 2004; Roming et al. 2005). For each of the six filters (UVW2, UVM2, UVW1, u, b, v), we processed the data by correcting for large scale sensitivity variations and masking bad pixels. Prior to stacking the data, we corrected each individual exposure for the time dependent detector sensitivity loss[8] and subtracted off the necessary counts to normalize the background count rate across exposures. Normalizing the background is especially important in the optical filters due to effects of scattered light from the Sun, Earth, and Moon. In total, the final stacked images included 151, 129, 136, 94, 24.3, 18.5 ks for the UVW2, UVM2, UVW1, u, b, and v filters respectively. The angular resolution of the UVOT filters is $\sim$2.″5.

As Swift was designed to study point sources, photometry must be done with care. Using the apertures defined in Section 2.1.1, we calculated the accumulated count rate as a function of radius, following Gil de Paz et al. (2007). This brightness profile was then used to determine the magnitude in each radial bin using the zero-point offsets from Breeveld et al. (2011). As discussed in Decleir et al. (2019) and Belles et al. (2023), the zero-point offsets are defined based on a 5 arcsec aperture. Therefore, we divided our measured fluxes by the asymptote of the curve of growth (Breeveld et al. 2010) in order to account for the difference in the effective aperture area. We used the Python package `dust_extinction`[9] and the "F99" dust model from Fitzpatrick (1999), along with A_V and E

[5] https://irsa.ipac.caltech.edu/Missions/wise.html
[6] https://irsa.ipac.caltech.edu/applications/2MASS/LGA/intro.html
[7] https://heasarc.gsfc.nasa.gov/cgi-bin/W3Browse/swift.pl
[8] https://heasarc.gsfc.nasa.gov/docs/heasarc/caldb/swift/docs/uvot/uvotcaldb_throughput_06.pdf
[9] https://dust-extinction.readthedocs.io/en/stable/

$(B-V)$ provided in Table 1, to correct the Swift flux densities for dust extinction and attenuation.

2.1.5. GALEX

We retrieved GALEX FUV and NUV imaging from the Mikulski Archive for Space Telescopes (MAST:10.17909/k7y9-yp18). The images were obtained on 2004 October 26, with a total exposure time of 12,987.6 s in both filters. The angular resolution is 4.3″ in the FUV and 5.3″ in the NUV, and images are in units of counts per second. Images are converted to flux density units of erg s^{-1} cm^{-2} $Å^{-1}$ by multiplying by 1.4×10^{-15} (FUV) or 2.06×10^{-16} (NUV; Martin et al. 2005; Morrissey et al. 2007). As for the Swift/UVOT observations (Section 2.1.4), the GALEX flux densities are corrected for Galactic dust extinction and attenuation.

2.2. Modeling the SED

Figure 2 shows a red, green, and blue (RGB)-rendered image of NGC 300 (using GALEX NUV, Spitzer 3.6 μm, and Spitzer 24 μm imaging in the blue, green, and red channels, respectively) with the elliptical annuli corresponding to a width of R_d superimposed (the locations of Chandra X-ray sources used in our XRB analysis are shown in yellow, while X-ray sources that are not used are shown in white; see Section 3). The D_{25} isophotal ellipse (de Vaucouleurs et al. 1991), shown in cyan for comparison, is slightly larger than the outer annular region. Table 2 provides the photometry measurements that are used to construct SEDs for the entire galaxy and the four subgalactic annuli. We use PROSPECTOR (Leja et al. 2017; Johnson et al. 2021)[10] to model the SEDs of NGC 300. PROSPECTOR forward-models the observed photometry given parameters that describe the gas, dust, and stellar populations present in the galaxy in addition to instrumental parameters. The code uses noise models and prior distributions to compute the likelihood and posterior probability for the given model and performs Monte Carlo sampling of the posterior probability distribution. PROSPECTOR has been extensively tested on SEDs and spectroscopy of nearby galaxies (Leja et al. 2017, 2018), dwarf galaxies (Greco et al. 2018; Pandya et al. 2018), and has been used in spatially resolved studies (Patrício et al. 2018; Oyarzún et al. 2019).

We use the nonparametric "continuity star formation history" (`continuity_sfh`) model (Leja et al. 2019; Johnson et al. 2021) to fit piecewise constant (or step function) SFHs in seven time bins. Rather than directly fitting for the SFR in each time bin, this model utilizes parameters that describe the ratio of SFRs in adjacent temporal bins. The default priors on these ratios are described by Student-t distributions and a Kroupa (2001) initial mass function (IMF). This model results in SFHs that tend toward constant SFRs, as dramatic differences in SFRs between adjacent temporal bins are down-weighted. We selected this SFH model given that NGC 300 shows no evidence of having undergone dramatic merger or interaction events that would lead to brief, high-SFR episodes. We adopt the same time bins as Leja et al. (2019): 0–30 Myr, 30–100 Myr, 100–330 Myr, 330 Myr–1.1 Gyr, 1.1–3.6 Gyr, 3.6–11.7 Gyr, and 11.7–13.7 Gyr. The first two bins are directly relevant to the current HMXB population, while the last time bin is selected to permit a maximally old population. The intermediate time bins spanning from 100 Myr to 11.7 Gyr are equally spaced in logarithmic time (see, e.g., Ocvirk et al. 2006).

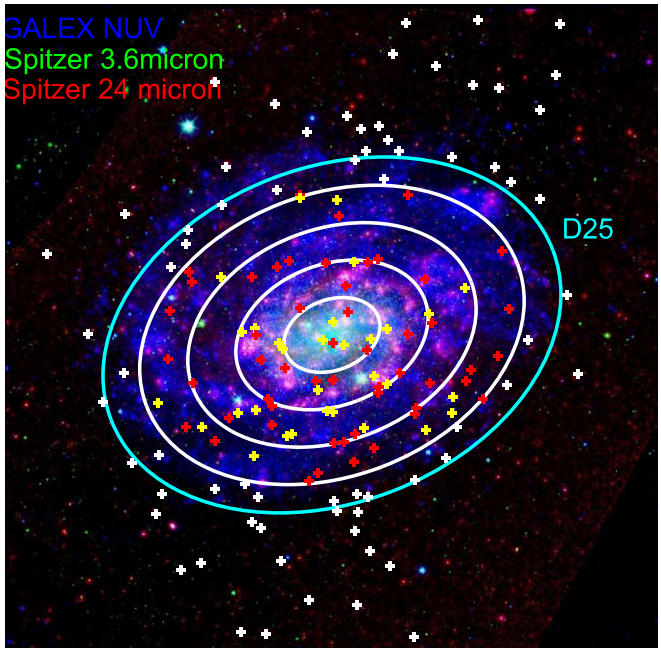

Figure 2. An RGB-rendered image of NGC 300, with the with four subgalactic regions shown by white elliptical annuli. The D_{25} isophote (de Vaucouleurs et al. 1991) is shown in cyan for comparison. The GALEX NUV image is shown in the blue channel, the Spitzer IRAC 3.6 μm is shown in green, and the Spitzer MIPS 24 μm is shown in red. Chandra X-ray sources that heavily absorbed and likely to be AGN are shown in red, sources that are consistent with being XRBs are shown as yellow crosses, and X-ray sources that are not used are shown as white crosses (see Section 3).

The metallicity, stellar mass formed, and dust attenuation optical depth ($\tau_{\rm dust}$) are additional free parameters in our model. Metallicity priors are assumed to be Gaussian. Although the slopes of the metallicity gradients reported by Kudritzki et al. (2008) and Gogarten et al. (2010) agree, their central metallicity values differ by $\sim0.3Z_{\odot}$ (see Table 3). The central metallicity value depends on the calibration used, and the value reported by Kudritzki et al. (2008) was derived from a combination of abundance estimates from mostly Fe, Ti, and Cr spectral lines. The color–magnitude diagram (CMD) fitting technique utilized by Gogarten et al. (2010) relies on the synthetic photometry of theoretical stellar isochrones to determine the best metallicity for a given stellar population. Given the consistency of the slopes, Gogarten et al. (2010) adopt the Kudritzki et al. (2008) central value when discussing the implications of the metallicity gradient. We initialized the metallicity prior by setting the mean value equal to the direct measurement value derived from Kudritzki et al. (2008) at each ring midpoint. The uncertainty in the metallicity is computed from the uncertainty in the observed metallicity gradient and the effect of the finite thickness of the radial bin added in quadrature; we set the standard deviation of the Gaussian prior to twice this metallicity uncertainty value (typically $\approx$0.3). This standard deviation was large enough to be inclusive of the Gogarten et al. (2010) values across the disk. We note that we obtained similar metallicity values when we used an uninformative prior on the metallicity, but we opted to retain the Gaussian prior on the metallicity as it decreased the amount of time required by PROSPECTOR to obtain a good fit.

[10] See also https://github.com/bd-j/prospector..

Table 2
UV, Optical, and IR Photometry of NGC 300

Instrument	Wavelength	Flux Densities				
		Whole Galaxy (Jy)	Inner (Jy)	Inner Middle (Jy)	Outer Middle (Jy)	Outer (Jy)
(1)	(2)	(3)	(4)	(5)	(6)	(7)
GALEX FUV	1535.08 Å	0.231 ± 0.003	0.026 ± 0.001	0.084 ± 0.001	0.067 ± 0.002	0.054 ± 0.003
Swift UVW2	2054.61 Å	0.261 ± 0.005	0.035 ± 0.001	0.096 ± 0.003	0.076 ± 0.003	0.056 ± 0.002
Swift UVM2	2246.43 Å	0.253 ± 0.005	0.034 ± 0.001	0.093 ± 0.003	0.074 ± 0.003	0.054 ± 0.002
GALEX NUV	2300.78 Å	0.316 ± 0.003	0.039 ± 0.001	0.111 ± 0.001	0.091 ± 0.003	0.074 ± 0.003
Swift UVW1	2580.74 Å	0.305 ± 0.007	0.047 ± 0.002	0.113 ± 0.004	0.086 ± 0.004	0.059 ± 0.004
Swift u	3467.05 Å	0.621 ± 0.007	0.099 ± 0.002	0.247 ± 0.005	0.158 ± 0.004	0.118 ± 0.003
Swift b	4349.56 Å	1.288 ± 0.028	0.247 ± 0.006	0.421 ± 0.013	0.351 ± 0.017	0.269 ± 0.018
Swift v	5425.33 Å	1.945 ± 0.018	0.421 ± 0.005	0.635 ± 0.009	0.508 ± 0.010	0.382 ± 0.011
2MASS *J*	1.235 μm	4.109 ± 0.069	1.065 ± 0.018	1.660 ± 0.018	1.024 ± 0.062	0.360 ± 0.068
2MASS *H*	1.662 μm	4.047 ± 0.064	1.076 ± 0.019	1.500 ± 0.019	1.018 ± 0.057	0.453 ± 0.063
2MASS K_s	2.159 μm	3.088 ± 0.054	0.811 ± 0.014	1.208 ± 0.014	0.742 ± 0.050	0.327 ± 0.053
WISE W1	3.4 μm	1.948 ± 0.004	0.458 ± 0.001	0.723 ± 0.003	0.494 ± 0.004	0.273 ± 0.005
Spitzer IRAC1	3.6 μm	1.857 ± 0.101	0.410 ± 0.016	0.750 ± 0.038	0.454 ± 0.090	0.243 ± 0.109
Spitzer IRAC2	4.5 μm	1.251 ± 0.049	0.285 ± 0.013	0.480 ± 0.045	0.304 ± 0.073	0.181 ± 0.086
WISE W2	4.6 μm	1.143 ± 0.004	0.266 ± 0.001	0.453 ± 0.004	0.278 ± 0.006	0.151 ± 0.006
Spitzer IRAC3	5.8 μm	1.115 ± 0.464	0.271 ± 0.121	0.507 ± 0.248	0.247 ± 0.109	<1.299
Spitzer IRAC4	8.0 μm	2.156 ± 0.034	0.500 ± 0.012	0.999 ± 0.023	0.453 ± 0.028	0.203 ± 0.031
WISE W3	12 μm	1.949 ± 0.097	0.434 ± 0.025	0.902 ± 0.057	0.419 ± 0.068	0.195 ± 0.080
WISE W4	22 μm	2.017 ± 0.765	0.465 ± 0.192	1.280 ± 0.413	0.510 ± 0.467	0.222 ± 0.133
Spitzer MIPS1	24 μm	1.993 ± 0.479	0.389 ± 0.128	1.092 ± 0.330	0.348 ± 0.186	<0.423
Spitzer MIPS2	70 μm	39.242 ± 2.878	7.333 ± 0.980	18.728 ± 0.134	8.680 ± 0.152	4.502 ± 0.167
Spitzer MIPS3	160 μm	144.855 ± 6.201	24.264 ± 2.997	57.777 ± 0.123	39.179 ± 0.139	23.635 ± 0.148

(This table is available in machine-readable form.)

Table 3
Previous Spatially Integrated Measurements of NGC 300 Physical Parameters

Method	Value	Reference
(1)	(2)	(3)
Star Formation Rate ($M_\odot$ yr^{-1})		
PROSPECTOR	0.177	this work
FUV+NUV	0.46	Mondal et al. (2019)
FUV	0.32	Lee et al. (2009)
UV	0.28	Kaisina et al. (2012)
CMD fitting	0.15	Gogarten et al. (2010)
Hα	0.14	Helou et al. (2004)
Hα	0.17	Kaisina et al. (2012)
NUV+70 μm	0.09	Mineo et al. (2012)
8 μm	0.08–0.11	Helou et al. (2004)
Stellar Mass ($M_\odot$)		
PROSPECTOR	2.15×10^9	this work
H I	4.2×10^9	Puche et al. (1990)
IR (S^{4}G)	2.1×10^9	Querejeta et al. (2015)
Optical+IR (S^{4}G)	2.0×10^9	Laine et al. (2016)
Central Metallicity ($Z/Z_\odot$)[a]		
PROSPECTOR	0.54	this work
12+log(O/H)	0.76	Bresolin et al. (2009)
12+log(O/H)	0.78	Micheva et al. (2022)
[M/H]	0.59	Gogarten et al. (2010)
$Z/Z_\odot$	0.87	Kudritzki et al. (2008)

Note.
[a] Metallicites have been converted to $Z/Z_\odot$ for ease of comparison.

NGC 300 is estimated to have a total stellar mass of $\sim 2.4 \times 10^9$ $M_\odot$ (Puche et al. 1990; Sheth et al. 2010; Querejeta et al. 2015). We assume this mass is distributed in the same manner as the 3.6 μm surface brightness profile when providing an initial estimate of the stellar mass contained in each radial bin, and we assume a log uniform prior on the stellar mass (with minimum and maximum stellar mass values set to 10^6 $M_\odot$ and 10^{10} $M_\odot$, respectively). The dust attenuation parameter assumes a flat (top-hat) prior with minimum and maximum values of 0.0 and 2.0. We experimented with changing the maximum and minimum values used by the dust attenuation and stellar mass priors, and with changing the initial values of the stellar mass and metallicity. Altering these values had no significant effect on the resulting fits. Changing the initial value of the stellar mass by up to a factor of ∼5 similarly did not significantly affect our results. The best-fit model was determined via χ^2 minimization, and parameter values around the best-fit were sampled with an ensemble MCMC algorithm (Goodman & Weare 2010) using the `emcee` Python package (Foreman-Mackey et al. 2013). We initialize `emcee` with 128 walkers and 512 iterations to build up a distribution of SED models. The best-fit parameters and uncertainties were defined by the 16th, 50th, and 84th percentile quantities of each distribution.

2.3. Comparison to Previous Studies

Table 3 provides an overview of the spatially integrated SFR, $M_\star$, and central metallicity[11] values reported for NGC 300 from the literature and our PROSPECTOR modeling; the detailed fit parameters and SFHs from PROSPECTOR are summarized in

[11] Bresolin et al. (2009) and Micheva et al. (2022) report 12+log(O/H). We convert to $Z/Z_\odot$ assuming $10^{X-8.69}$ (Asplund et al. 2009), where X is the reported 12+log(O/H) value.

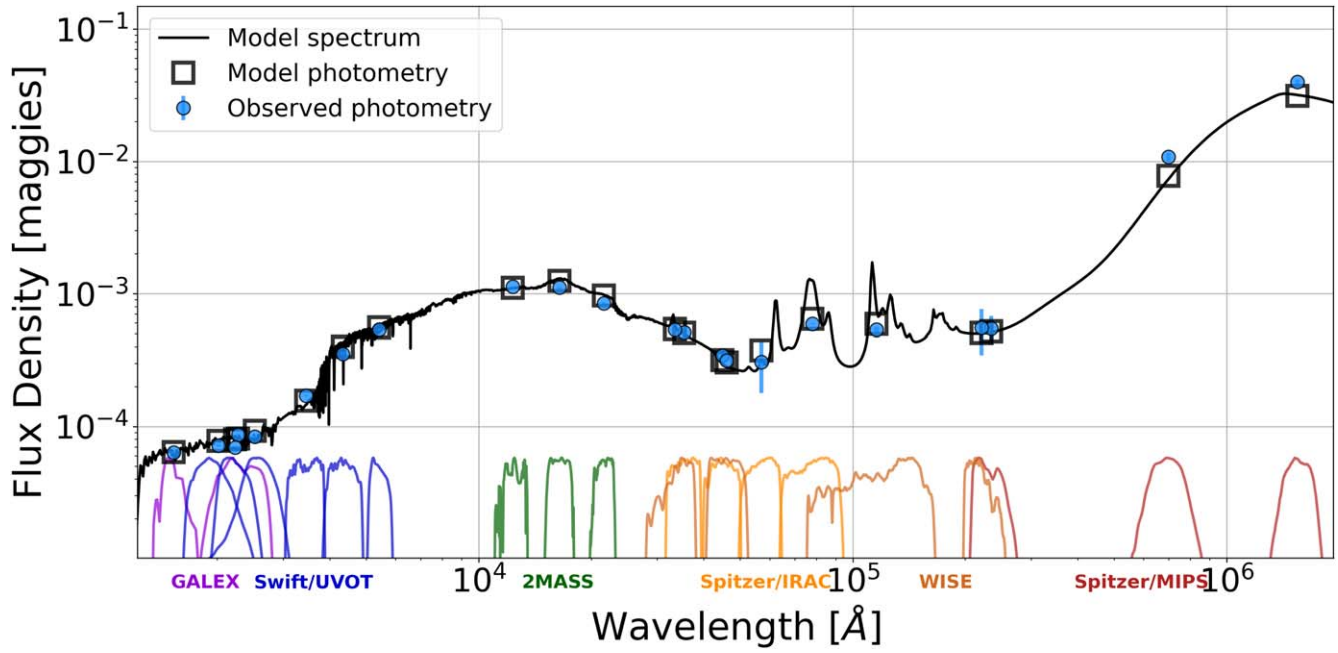

Figure 3. The best-fit, whole-galaxy (out to $4R_d$) SED for NGC 300. The observed photometry (from Table 2) is shown as blue dots. The best-fit model spectrum is shown in black, and black open squares indicate the model-predicted photometry for each filter used. The filter transmission curves are shown in multiple colors across the lower horizontal axis.

Table 4
Best-fit SED Models from PROSPECTOR

Parameter	Units	Galaxy Integrated	Radial Bin				Sum of All Radial Bins
		($\leqslant 4R_d$)	$\leqslant R_d$	$R_d < r \leqslant 2R_d$	$2R_d < r \leqslant 3R_d$	$3R_d < r \leqslant 4R_d$	
(1)	(2)	(3)	(4)	(5)	(6)	(7)	(8)
$M_\star$	$10^9\ M_\odot$	$2.15^{+0.26}_{-0.14}$	$0.64^{+0.03}_{-0.02}$	$0.94^{+0.08}_{-0.07}$	$0.38^{+0.06}_{-0.04}$	$0.27^{+0.03}_{-0.02}$	$2.23^{+0.20}_{-0.15}$
SFR(<100 Myr)	$M_\odot\ \mathrm{yr}^{-1}$	0.177 ± 0.070	$0.016^{+0.009}_{-0.007}$	$0.094^{+0.026}_{-0.033}$	$0.045^{+0.035}_{-0.026}$	$0.014^{+0.011}_{-0.006}$	$0.169^{+0.081}_{-0.072}$
log(Z)	$\log[Z_\odot]$	$-0.239^{+0.014}_{-0.033}$	$-0.266^{+0.017}_{-0.013}$	-0.360 ± 0.013	$-0.459^{+0.065}_{-0.046}$	$-0.628^{+0.011}_{-0.012}$	...
τ_{dust}	...	$0.122^{+0.008}_{-0.005}$	$0.155^{+0.007}_{-0.009}$	0.170 ± 0.007	$0.145^{+0.009}_{-0.008}$	0.122 ± 0.09	...
Star Formation History							
0–30 Myr	$M_\odot\ \mathrm{yr}^{-1}$	0.048 ± 0.018	$0.005^{+0.003}_{-0.002}$	$0.016^{+0.007}_{-0.005}$	$0.017^{+0.007}_{-0.006}$	$0.013^{+0.005}_{-0.004}$	$0.051^{+0.022}_{-0.017}$
30–100 Myr	$M_\odot\ \mathrm{yr}^{-1}$	$0.234^{+0.094}_{-0.093}$	$0.021^{+0.012}_{-0.009}$	$0.128^{+0.034}_{-0.046}$	$0.057^{+0.034}_{-0.048}$	$0.014^{+0.013}_{-0.007}$	$0.220^{+0.093}_{-0.110}$
100–330 Myr	$M_\odot\ \mathrm{yr}^{-1}$	$0.462^{+0.231}_{-0.086}$	$0.070^{+0.015}_{-0.029}$	$0.161^{+0.082}_{-0.045}$	$0.105^{+0.035}_{-0.048}$	$0.068^{+0.032}_{-0.045}$	$0.404^{+0.164}_{-0.167}$
330 Myr–1.1 Gyr	$M_\odot\ \mathrm{yr}^{-1}$	$0.263^{+0.056}_{-0.085}$	$0.065^{+0.015}_{-0.012}$	$0.053^{+0.023}_{-0.027}$	$0.044^{+0.023}_{-0.024}$	$0.093^{+0.033}_{-0.024}$	$0.255^{+0.094}_{-0.087}$
1.1–3.6 Gyr	$M_\odot\ \mathrm{yr}^{-1}$	$0.239^{+0.064}_{-0.096}$	$0.017^{+0.015}_{-0.010}$	$0.066^{+0.027}_{-0.023}$	$0.126^{+0.025}_{-0.029}$	$0.030^{+0.013}_{-0.010}$	$0.239^{+0.080}_{-0.072}$
3.6–11.7 Gyr	$M_\odot\ \mathrm{yr}^{-1}$	$0.239^{+0.041}_{-0.034}$	$0.100^{+0.009}_{-0.010}$	$0.087^{+0.024}_{-0.023}$	$0.023^{+0.013}_{-0.018}$	$0.022^{+0.007}_{-0.005}$	$0.232^{+0.053}_{-0.056}$
11.7–13.7 Gyr	$M_\odot\ \mathrm{yr}^{-1}$	$0.222^{+0.276}_{-0.078}$	$0.055^{+0.053}_{-0.043}$	$0.261^{+0.163}_{-0.116}$	$0.007^{+0.005}_{-0.009}$	$0.032^{+0.032}_{-0.015}$	$0.355^{+0.253}_{-0.183}$
Stellar Mass Formation History							
0–30 Myr	$\log[M_\odot]$	$6.14^{+0.14}_{-0.20}$	5.18 ± 0.19	5.67 ± 0.15	$5.69^{+0.13}_{-0.23}$	$5.58^{+0.14}_{-0.17}$	$6.17^{+0.14}_{-0.23}$
30–100 Myr	$\log[M_\odot]$	$7.21^{+0.15}_{-0.22}$	$6.16^{+0.20}_{-0.25}$	$6.95^{+0.10}_{-0.19}$	$6.60^{+0.26}_{-0.39}$	$6.00^{+0.29}_{-0.27}$	$7.19^{+0.24}_{-0.30}$
100–330 Myr	$\log[M_\odot]$	$8.03^{+0.18}_{-0.09}$	$7.21^{+0.09}_{-0.24}$	$7.57^{+0.18}_{-0.14}$	$7.39^{+0.16}_{-0.17}$	$7.19^{+0.17}_{-0.47}$	$7.97^{+0.16}_{-0.21}$
330 Myr–1.1 Gyr	$\log[M_\odot]$	$8.30^{+0.08}_{-0.17}$	7.70 ± 0.09	$7.61^{+0.16}_{-0.31}$	$7.53^{+0.19}_{-0.32}$	7.85 ± 0.13	$8.29^{+0.14}_{-0.18}$
1.1–3.6 Gyr	$\log[M_\odot]$	$8.78^{+0.10}_{-0.22}$	$7.64^{+0.28}_{-0.37}$	$8.22^{+0.15}_{-0.19}$	$8.51^{+0.09}_{-0.10}$	$7.88^{+0.15}_{-0.17}$	8.78 ± 0.14
3.6–11.7 Gyr	$\log[M_\odot]$	9.29 ± 0.07	$8.91^{+0.04}_{-0.05}$	$8.85^{+0.10}_{-0.13}$	$8.28^{+0.25}_{-0.36}$	$8.26^{+0.09}_{-0.16}$	$9.07^{+0.09}_{-0.10}$
11.7–13.7 Gyr	$\log[M_\odot]$	$8.66^{+0.19}_{-0.35}$	$8.05^{+0.29}_{-0.68}$	$8.73^{+0.21}_{-0.26}$	$7.17^{+0.61}_{-0.35}$	$7.82^{+0.30}_{-0.26}$	$8.86^{+0.25}_{-0.30}$

Table 4. We additionally provide the stellar mass formation history, which is the SFR in each time bin integrated over the duration of the time bin. This gives a measure of the total mass in stars that formed in each epoch; the current stellar mass $M_\star$ represents the surviving stellar mass at the present time and is lower than the total mass formed in stars. The best-fit SED parameters for the spatially integrated SED and the radial subgalactic regions are modeled independently; i.e., column (3) of Table 4 is not the sum of columns (4)–(7). We note that the sums of the stellar masses and SFRs over the subgalactic regions yield values that are generally within 2σ of the value derived from the spatially integrated SED. Figure 3 shows the

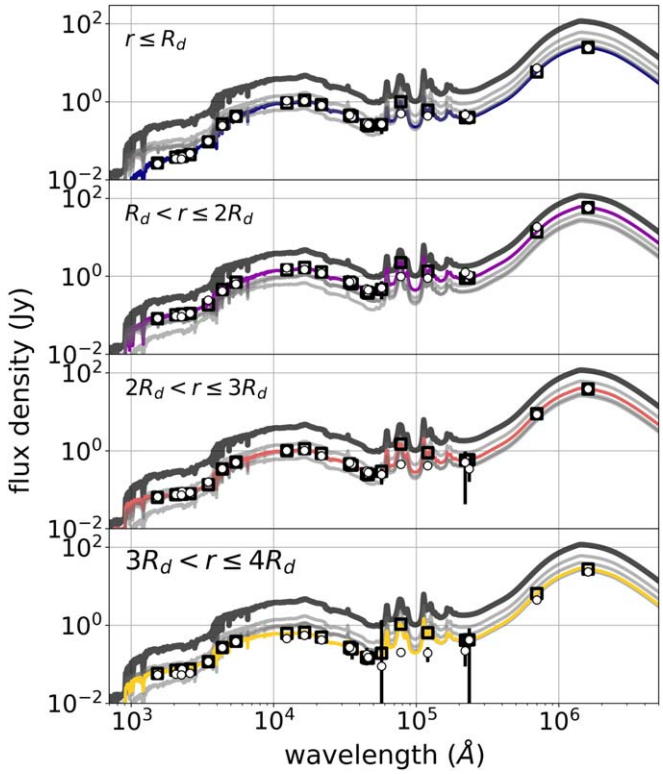

Figure 4. Best-fit radial SEDs from PROSPECTOR. All four SEDs are shown in each plot in gray, with the relevant subregion highlighted in bold color. The galaxy-integrated best-fit SED model from Figure 3 is shown by the thick, dark gray line. The white circles show the photometry measurements from Table 2; in most cases, the uncertainties are smaller than the plotting symbol. Black squares show the predicted flux density in each filter.

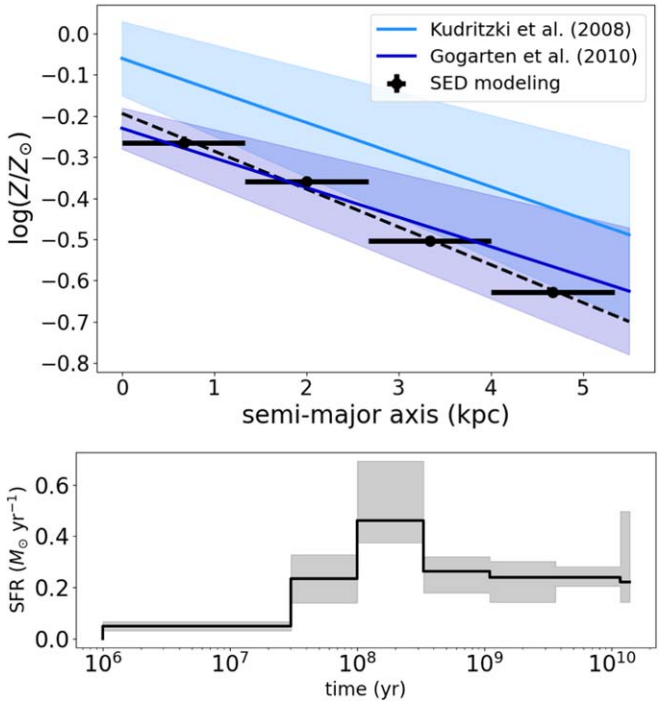

Figure 5. Top: The metallicity gradient of NGC 300. The black points show the results of our SED modeling with PROSPECTOR, and the dashed black line shows the best-fit metallicity gradient. The metallicity gradients taken from the literature (and their corresponding uncertainties) are shown in light blue (Kudritzki et al. 2008) and dark blue (Gogarten et al. 2010). Bottom: the SFH of NGC 300 (black; gray shaded region indicates uncertainties).

UV-to-IR galaxy-integrated SED of NGC 300 (out to $4R_d$) along with the best-fit model from PROSPECTOR, while Figure 4 shows the best SED models and the corresponding UV-IR photometry for the four subgalactic radial bins. The best-fit model for the entire galaxy yields a stellar mass, recent (<100 Myr) SFR, and metallicity that are all consistent with values previously reported in the literature (and summarized in Table 3).

The metallicity gradient recovered from the PROSPECTOR is shown in the top panel of Figure 5 compared to the gradients of Kudritzki et al. (2008, light blue) and Gogarten et al. (2010, dark blue). Our SED modeling of NGC 300 yields a metallicity gradient of

$$\log(Z/Z_\odot) = (-0.193 \pm 0.016) - (0.092 \pm 0.005)r, \quad (2)$$

where r is the galactocentric radius in kiloparsecs. This gradient shows good agreement with those taken from the literature and predicts a central metallicity value that is intermediate between the Gogarten et al. (2010) and Kudritzki et al. (2008) values. Our utilization of PROSPECTOR is similar to CMD fitting in that we rely on similar theoretical stellar models to construct galaxy SEDs for comparison to flux densities, rather than directly fitting for abundances from spectra. We note that the radial gradient obtained by Gogarten et al. (2010) was derived using a narrow strip of three HST fields that spanned the disk of NGC 300 (which also prohibited the measurement of integrated galaxy mass and SFR), while our SED modeling uses observations extending over the full annular rings shown in Figure 2. The metallicity gradient of NGC 300 from Kudritzki et al. (2008) was derived from a sample of 24 supergiants (with spectral types ranging from B8 to A4), and Bresolin et al. (2009) found that these direct stellar metallicity measurements were in excellent agreement with those derived from a sample of 28 H II regions for which auroral lines were detected. The stellar and auroral nebular metallicities did not, however, agree with abundances derived from strong-line methods: the metallicity gradient based on strong oxygen lines in Zaritsky et al. (1994) and Deharveng et al. (1988) ∼50% steeper than that found in Kudritzki et al. (2008) and Bresolin et al. (2009). The metallicities of H II regions in two other well-studied spiral galaxies, the Milky Way and M33, show significant discrepancies depending on the lines and methods used, and these differences cannot be explained by measurement errors. Using mid- and far-IR lines largely resolves the discrepancies in the Milky Way (Martín-Hernández et al. 2002; Rudolph et al. 2006), bringing the nebular metallicity gradient into agreement with that of direct stellar measurements, but these lines are rarely used to derive metallicities or abundance gradients in external spiral galaxies. Metallicity and its role in HMXB evolution is discussed further in Section 4.

The overall SFH for the entire galaxy (Figure 5, bottom panel) is in broad agreement with previous studies, showing an enhancement in the SFR at early times (roughly 90% the stars ever formed in NGC 300 were formed more than a few Gyr ago, as found by Gogarten et al. 2010). The average SFR on timescales relevant for HMXBs (<100 Myr) agrees with estimates derived by other SFR indicators; our SED modeling suggests that most of the star formation activity occurred

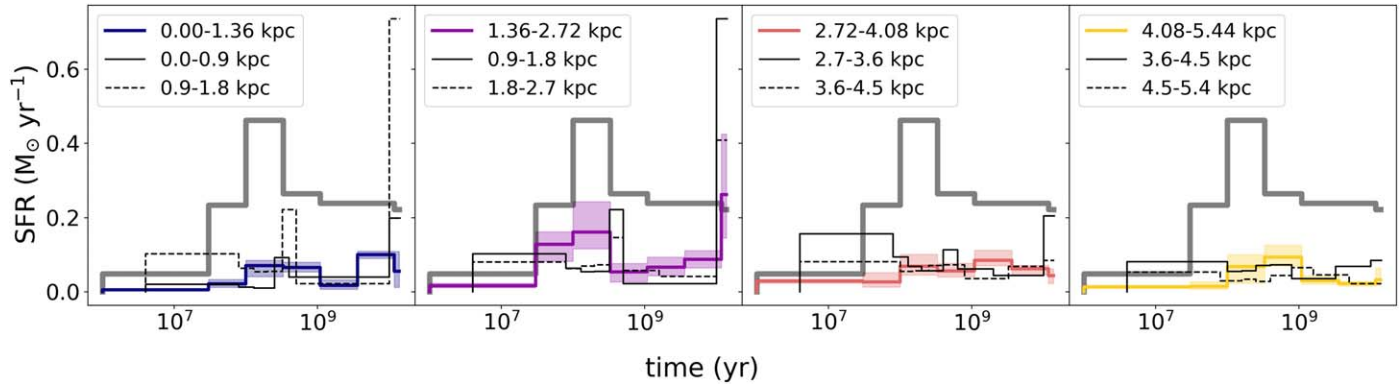

Figure 6. Radially resolved SFHs derived from PROSPECTOR modeling (color-coded as in Figure 4) with increasing galactocentric radius (from left to right) compared to the SFHs derived by Gogarten et al. (2010, solid and dashed black lines) at similar galactocentric distances. The SFHs from Gogarten et al. (2010) carry a typical uncertainty of ∼10%–20% and were computed over a much smaller surface area of NGC 300 than the PROSPECTOR-derived SFHs. The galaxy-integrated SFH from Figure 5 is shown by the thick gray line.

∼30–100 Myr ago, with the most recent SFR (<30 Myr) occurring at only ∼20% the rate found for the older time bin. Williams et al. (2013) found that most HMXBs in NGC 300 are ∼40–60 Myr old through CMD analysis of the resolved stellar populations in the vicinity of HMXB candidates, with NGC 300 ULX-1 being the only notable exception of a younger HMXB (the massive HMXB NGC 300 X-1 is likely <30 Myr as well, given the large BH mass and evolved state of the Wolf–Rayet companion; Binder et al. 2020, 2021). We next compared the SFHs derived by PROSPECTOR to the radially resolved SFHs of Gogarten et al. (2010), which assumed a Salpeter (1955) IMF during CMD fitting but report results scaled to a Kroupa (2001) IMF. Although the outermost radii (∼5.4 kpc) are similar in both studies, we use four bins each with a width of 1.36 kpc while Gogarten et al. (2010) used six bins of a width of 0.9 kpc, and the time bins used in constructing the SFHs differ. Furthermore, the Gogarten et al. (2010) analysis was limited to the small area covered by the HST fields, whereas our SED modeling is performed for annular rings across the entire disk. This introduces some additional uncertainty in the comparison of the two radially resolved SFHs. The SFHs show broad agreement (uncertainties in the Gogarten et al. 2010 SFRs are typically on the order of ∼20%; Figure 6), with the largest discrepancies appearing in the oldest time bin at $r < 2R_d$, where Gogarten et al. (2010) predict a higher SFR at very early times compared to our PROSPECTOR results, particularly at $r \lesssim 4$ kpc. These differences will not affect our interpretation of the HMXB population properties, which depend only on the most recent SFRs.

Different SFR indicators are sensitive to different population ages, and Kouroumpatzakis et al. (2020) demonstrated that the relationship between L_X and SFR of HMXB populations depends on choice of SFR indicator. As shown in Table 3, different SFR indicators can yield up to a factor of ∼5 difference in inferred SFR in NGC 300 on a galaxy-integrated scale. Metallicity, too, can be measured through a variety of means; nearly all studies of the L_X–SFR–Z relationship assume the overall metallicity of a galaxy is well traced by the nebular oxygen abundance, 12 + log (O/H). While emission lines from H II region spectra provide the bulk of direct present-day abundance measurements, many studies utilize metallicities derived from strong-line indices such as [O III] λ5007. Auroral emission lines that directly probe both the composition and the electron temperatures of H II regions (e.g., [O III] λ4363) become fainter with both increasing distance and metallicity (as the electron temperature decreases due to cooling via metal lines; Berg et al. 2015; Croxall et al. 2015, 2016), eventually becoming to faint to detect. Strong-line metallicity indices therefore depend either on empirical calibrations tied to more local auroral line measurements (Pettini & Pagel 2004; Pilyugin & Thuan 2005; Liang et al. 2007; Florido et al. 2022) or theoretical calibrations derived from grids of photoionization models (McGaugh 1991; Kewley & Dopita 2002; Tremonti et al. 2004). These different calibrations provide large differences (∼0.7 dex) in the inferred metallicities (Kewley & Ellison 2008), and may be significantly contributing to the observed scatter in the L_X–SFR–Z relationships.

3. X-Ray Observations from Chandra

We retrieved four Chandra ACIS-I observations (observation IDs, hereafter ObsIDs, 12238, 16028, 16029, and 22375) from the Chandra archive.[12] The observations ranged in exposure duration from 47.4 ks (ObsID 22375) to 64.2 ks (ObsID 16028). We reprocessed all `evt1` data using the CIAO v4.15 (Fruscione et al. 2006) task `chandra_repro` and standard reduction procedures. We ran the point-source detection algorithm `wavdetect` on each individual exposure to generate a preliminary list of X-ray source positions and error ellipses. The major and minor axes of these error ellipses were increased by a factor of 5, and all X-ray sources were masked so that a background light curve could be extracted for each observation. We inspected these background light curves but found no evidence for strong, prolonged background flaring events in any of the four observations. We created good time intervals (GTIs) using `lc_clean` and filtered all event data on these GTIs. Finally, we restricted the energy range of our resulting "clean" `evt2` files to 0.5–7 keV.

We updated the absolute astrometry of all four images by using the tasks `wcs_match` and `wcs_match` to align each Chandra observation to the longest observation (ObsID 16028). Images were finally reprojected to a common tangent point and combined using the CIAO task `reproject_obs` and `flux_obs`. The total usable Chandra exposure time was 235.9 ks. We next reran `wavdetect` on the merged observation, using smoothing scales of "1 2 4 8" and a significance threshold of 10^{-6}. A total of 154 X-ray sources were detected in the merged Chandra image. An RGB-rendered image of NGC 300 with the locations of all Chandra X-ray

[12] https://cda.harvard.edu/chaser/

sources is shown in Figure 2. A summary of the properties of all the detected X-ray sources is provided in Table 5 and provided as a machine-readable table from the journal.

We additionally calculate hardness ratios for each X-ray source using the Bayesian estimation of hardness ratios (BEHR) code (Park et al. 2006) following the same methodology as in Binder et al. (2012). We define two hardness ratios,

$$\mathrm{HR1} = \frac{M - S}{H + M + S}, \quad (3)$$

and

$$\mathrm{HR2} = \frac{H - M}{H + M + S}, \quad (4)$$

where S is the "soft" band (0.35–1.1 keV), M is the "medium" band (1.1–2.6 keV), and H is the "hard" band (2.6–8.0 keV). We use BEHR to generate 50,000 samples of the source flux probability distributions (in all four observations) for each of the three bands, which we use to compute 50,000 values of HR1 and HR2 for each source. In Table 5, we report the median value for each hardness ratio, and the uncertainties are defined using the 16th and 84th percentile values. We use the hardness ratio categories defined in Binder et al. (2012) to roughly classify sources as likely XRBs, supernova remnants (SNRs), highly absorbed sources ("ABS"), indeterminate soft or hard sources ("SOFT" and "HARD," respectively), and sources with indeterminate spectral types ("INDET"). The hardness ratio diagram in Figure 7 shows the hardness ratios for each source and the six categories defined in Binder et al. (2012).

3.1. Sensitivity Curves and Limiting Fluxes

In addition to generating a merged observation image, we also created background images using the CIAO `blank_sky` task. "Blank sky" images were generated to estimate the source-free background across the detector for each observation and merged in the same manner as described above for the actual observation images. These blank sky images can be used to derive sensitivity curves, which provide an estimate of the probability that an X-ray source with a given flux will be detected at a given location on the detector. These are essential components for accurately modeling XLFs and for determining the flux levels below which a source catalog is highly incomplete.

We follow the methodology of Georgakakis et al. (2008) to construct a sensitivity curve for the merged Chandra image of NGC 300. We present a summary of the sensitivity curve construction procedure here; the reader is referred to Georgakakis et al. (2008) for additional details and an example application to AGN observations. The merged blank sky image provides us with an estimate of the mean expected source-free background counts B across the entire image. The cumulative probability that the observed number of counts detected in a source (which is a sum of the counts intrinsic to the source and the background) will exceed some limit L is given by

$$P_B(\geqslant L) = \frac{1}{\Gamma(L)} \int_0^B e^{-t} t^{L-1} dt \quad (5)$$

assuming B and L are integers. If one adopts a value for the threshold probability P_B, Equation (5) can be inverted to find the detection limit L for a given background. We adopt a threshold probability of $P_B = 4 \times 10^{-6}$ (the values assumed by, e.g., Georgakakis et al. 2008; Laird et al. 2009, which corresponds to approximately 0.5 false sources per Chandra image) and perform this calculation across the entire merged image area to construct a map of L values as a function of (x, y), given the background counts B predicted by the blank sky map. We can convert L to an energy flux by assuming a power-law spectral model (with photon index $\Gamma = 1.7$ and subject to the Galactic absorbing column) and using the total exposure time at each (x, y) position across the image. From the resulting 2D fluxed image, we measure the total area over which a source with a given flux could be detected.

We perform this calculation for the whole galaxy out to a maximum distance of $4R_d$ (we note that beyond this radius the X-ray point-source population is likely to be both highly incomplete due to the lower sensitivity at large off-axis angle and dominated by background AGN, rather than sources intrinsic to NGC 300). The 90% limiting 0.5–7 keV flux is 3.38×10^{-15} erg s^{-1} cm^{-2} (corresponding to a luminosity of 1.6×10^{36} erg s^{-1} at the distance of NGC 300, in good agreement with Binder et al. 2012, 2017, who used a subset of the observations analyzed in this work but a somewhat less restrictive threshold for detection). We hereafter refer to the 90% limiting luminosity as $L_{X,90}$ and the 90% limiting flux as $S_{X,90}$.

For the remainder of our analysis, we only keep X-ray sources that meet all of the following three criteria: (1) detected at $r \leqslant 4R_d$, (2) detected at $\geqslant 3\sigma$ significance by `wavdetect`, and (3) with fluxes $\geqslant S_{X,90}$. Within $4R_d$, there is one supernova remnant (Gross et al. 2019) and one foreground star (Binder et al. 2012) that we remove from the X-ray source list. A total of 70 X-ray sources meet these criteria, with six located in the inner region, 16 in the inner middle bin, 22 in the outer middle bin, and 26 in the outer bin. These sources are indicated in yellow on Figure 2.

3.2. The X-Ray Binary Population

To estimate the number and total L_X produced by XRBs in NGC 300, we first used the AGN log$N$-log$S$ distribution from the Chandra Multiwavelength Project (ChaMP; Kim et al. 2004) to estimate the AGN contribution in each annular region. We estimate 43 ± 2 AGN above $S_{X,90}$ are found within the full survey area ($\leqslant 4R_d$), and $\sim$7 of these are AGN with fluxes above $\sim 2.1 \times 10^{-14}$ erg s^{-1} cm^{-2} (which corresponds to a luminosity of 10^{37} erg s^{-1} at the distance of NGC 300). The remaining $\sim$27 X-ray sources above $S_{X,90}$ ($\sim$6 above 10^{37} erg s^{-1}) are therefore likely intrinsic to NGC 300.

When we use the area spanned by each elliptical annulus, the predicted number of AGN above $S_{X,90}$ in each subgalactic radial bin (from the innermost region outward) is approximately 3, 8, 14, and 18. Given their far distance, background AGN are more likely to be highly absorbed than XRBs and other X-ray sources intrinsic to NGC 300; we therefore examine the number of sources with hardness ratios placing them in the "ABS" category of Figure 7 in at least one observation. We find 3, 13, 16, 20 sources show evidence of high absorption in each of the four radial bins. This is only slightly higher than the predicted number of background AGN, and consistent with expectations given that some XRBs can experience significant intrinsic absorption. We therefore expect approximately three, eight, eight, and eight X-ray sources above $S_{X,90}$ in the inner, inner middle, outer middle, and outer bin, respectively, are XRBs in NGC 300. We additionally

Table 5
Properties of All 154 X-Ray Sources Detected in Merged Chandra Image

RA	Decl.	Galactocentric Radius	Galactocentric Radius/Rd	Source Signif.	Net Counts	12238		16028		16029		22375	
(J2000)		(kpc)		(σ)	(0.5–7 keV)	HR1	HR2	HR1	HR2	HR1	HR2	HR1	HR2
13.6980206	−37.8927248	10.10	7.43	20.5	549 ± 35	⋯	⋯	⋯	⋯	⋯	⋯	$0.42^{+0.05}_{-0.05}$	$-0.20^{+0.06}_{-0.06}$
13.7722944	−37.8583461	8.07	5.93	4.2	35 ± 9	⋯	⋯	⋯	⋯	$0.75^{+0.12}_{-0.12}$	$-0.60^{+0.21}_{-0.22}$	⋯	⋯
13.6859116	−37.8505873	8.22	6.04	13.9	179 ± 18	⋯	⋯	$0.47^{+0.10}_{-0.10}$	$-0.33^{+0.14}_{-0.15}$	$0.44^{+0.08}_{-0.08}$	$-0.33^{+0.10}_{-0.11}$	⋯	⋯
13.6999274	−37.8355104	7.37	5.42	11.3	106 ± 13	⋯	⋯	$0.43^{+0.15}_{-0.14}$	$-0.31^{+0.19}_{-0.22}$	$0.40^{+0.10}_{-0.10}$	$-0.15^{+0.13}_{-0.15}$	⋯	⋯
13.7920276	−37.8333377	6.91	5.08	7.2	68 ± 12	⋯	⋯	⋯	⋯	$0.76^{+0.15}_{-0.19}$	$-0.78^{+0.23}_{-0.14}$	$0.28^{+0.21}_{-0.21}$	$-0.24^{+0.27}_{-0.30}$
13.8005427	−37.8284841	6.71	4.93	16.1	177 ± 17	⋯	⋯	⋯	⋯	$0.53^{+0.09}_{-0.09}$	$-0.30^{+0.13}_{-0.14}$	$0.47^{+0.08}_{-0.08}$	$-0.08^{+0.13}_{-0.14}$
13.7174112	−37.8202939	6.50	4.78	5.6	49 ± 10	⋯	⋯	$0.41^{+0.22}_{-0.21}$	$-0.18^{+0.30}_{-0.36}$	$0.56^{+0.22}_{-0.22}$	$-0.44^{+0.35}_{-0.32}$	$0.22^{+0.49}_{-0.48}$	$-0.08^{+0.65}_{-0.63}$
13.6970791	−37.8204055	6.68	4.91	4.4	35 ± 9	⋯	⋯	$0.45^{+0.19}_{-0.16}$	$-0.01^{+0.31}_{-0.37}$	$0.70^{+0.17}_{-0.18}$	$-0.58^{+0.29}_{-0.26}$	⋯	⋯
13.7205749	−37.8120096	6.09	4.48	4.6	53 ± 13	⋯	⋯	$0.52^{+0.20}_{-0.19}$	$-0.53^{+0.26}_{-0.23}$	$0.44^{+0.26}_{-0.28}$	$-0.29^{+0.40}_{-0.40}$	$-0.01^{+0.53}_{-0.54}$	$-0.34^{+0.34}_{-0.31}$
13.7953472	−37.8095754	5.85	4.30	34.4	416 ± 23	⋯	⋯	$0.42^{+0.11}_{-0.11}$	$-0.53^{+0.13}_{-0.13}$	$0.36^{+0.06}_{-0.07}$	$-0.36^{+0.07}_{-0.07}$	$0.51^{+0.06}_{-0.06}$	$-0.33^{+0.08}_{-0.08}$

Note.

Note. The entire table is published only in the electronic edition of the article. The first 10 lines are shown here for guidance regarding its form and content.

(This table is available in its entirety in machine-readable form.)

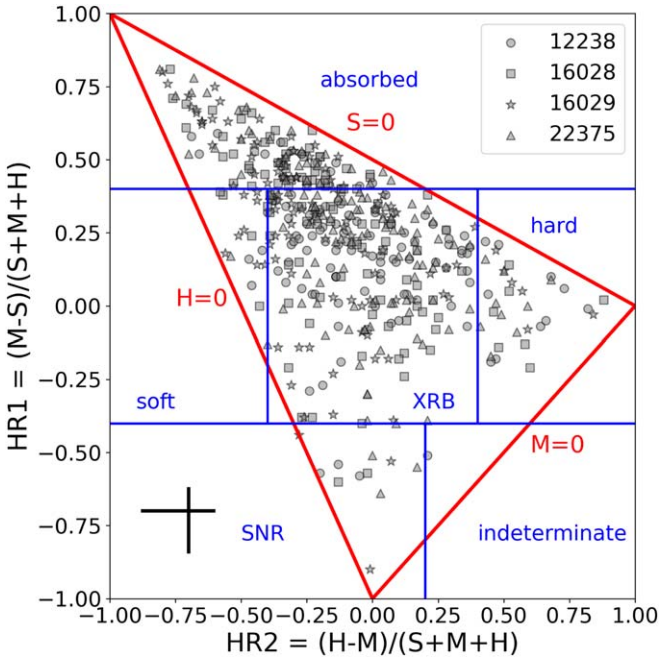

Figure 7. Hardness ratio diagram for all 154 sources detected in the merged Chandra image of NGC 300, with the six hardness ratio categories defined in Binder et al. (2012) shown in blue. Red lines indicate the physically meaningful region of the diagram. The typical uncertainty on the hardness ratios is shown by the black cross in the lower left corner.

measure the total flux we expect to originate from AGN and subtract this value from the flux of the total X-ray source population; the remainder is the approximate flux of XRBs in NGC 300. We use the reported uncertainties on the ChaMP log$N$-log$S$ distribution to assess the uncertainty in the number of AGN predicted in our observations; the uncertainty is ∼2–3 AGN for the whole galaxy. These calculations are summarized in Table 6.

Given the relatively low number of likely XRBs observed in each radial bin, we do not attempt to directly fit the XRB XLFs. Instead, we predict the expected number of HMXBs and LMXBs and their total L_X using the (metallicity-independent) HMXB and LMXB scaling relations of Lehmer et al. (2020, 2021):

$$\log\left(\frac{L_X^{\rm HMXB}}{\rm SFR}\right) = 39.71^{+0.14}_{-0.09}\left[\frac{\rm erg\ s^{-1}}{M_\odot\ \rm yr^{-1}}\right]$$
$$\log\left(\frac{L_X^{\rm LMXB}}{M_\star}\right) = 29.25^{+0.07}_{-0.06}\left[\frac{\rm erg\ s^{-1}}{M_\odot}\right]. \quad (6)$$

These scaling relations were derived from a sample of 24 elliptical galaxies (Lehmer et al. 2020) and 33 star-forming (average SFR∼1.4 $M_\odot$), HMXB-dominated galaxies (Lehmer et al. 2021). The XLFs of some of these galaxies extend below 10^{37} erg s^{-1} (4 out of 22 elliptical galaxies had 90% limiting luminosities below 10^{37} erg s^{-1}, and 9 out of 33 star-forming galaxies had 50% limiting luminosities comparable to $L_{X,90}$ in this work; Lehmer et al. 2020, 2021); however, the majority of the X-ray sources used to derive these scaling relations were significantly brighter than most of the X-ray sources coincident with the disk of NGC 300. Given the relatively small number of galaxies with X-ray source populations imaged to faint fluxes, the applicability of these scaling relations to faint XRB populations may be limited (see Section 4 for further discussion).

Since the SFRs and stellar masses considered here are low and XRB formation is a stochastic process, we use the following approach to estimate the XRB population properties expected for NGC 300. First, we randomly draw values of the SFR and $M_\star$ from within the uncertainties derived from our SED modeling for each subgalactic region in NGC 300 assuming a normal distribution with the mean set equal to the best-fit value of each parameter. Since our best-fit values of the SFR and $M_\star$ have asymmetric errors, we set the standard deviation of this normal distribution to the larger uncertainty. We then randomly select a value from within the uncertainties of the above scaling relations and compute the expected L_X for each population. To convert the predicted total L_X into a number of XRBs, we assume that both HMXBs and LMXBs follow the broken power-law models described in Lehmer et al. (2019, 2020).

To randomly generate a sample of synthetic XRBs that follow a broken power-law distribution, we follow the approach outlined in Clauset et al. (2009, Appendix D). We first generate a random L_X value for an XRB according to $L_{X,r} = L_{X,\,90}(1-r)^{-1/(\gamma_1-1)}$, where γ_1 is the faint-end power-law slope, and r is a number that is randomly drawn from a uniform distribution in the range $0 \leqslant r < 1$. If $L_{X,r}$ is brighter than the 10^{39} erg s^{-1} cutoff luminosity assumed in Lehmer et al. (2019, 2020), it is rejected. If $L_{X,r}$ is within the observed range of L_X values as the true sample, we draw a second uniform random variate r_2 (also in the range $0 \leqslant r_2 < 1$) and accept $L_{X,r}$ if $(L_{X,r}/L_{X,90})^{-\gamma_1} \geqslant r_2$. If $L_{X,r}$ is rejected, we use a similar functional form as above to generate a new value of $L_{X,r}$ that follows the bright end of the XLF: $L_{X,r} = L_{X,\,\rm break}(1-r)^{-1/(\gamma_2-1)}$, where γ_2 is the slope of the bright end of the XLF, and $L_{X,\,\rm break}$ is the break luminosity (3×10^{37} erg s^{-1} for LMXBs, and 10^{38} erg s^{-1} for HMXBs; Lehmer et al. 2019, 2020). Synthetic XRBs are generated one at a time, and their total luminosity is tracked until the value predicted using the scaling relations and relevant SFR and $M_\star$ values is obtained. This process is repeated 10,000 times to build up a distribution of synthetic HMXB and LMXB populations that satisfy the scaling relations in Equation (6) for the subgalactic regions of NGC 300. We used the median and 90% confidence interval to define the "predicted" number of XRBs and their collective L_X and report these values in Table 6. For clarity, we use use N and L_X to refer to numbers of X-ray sources and their luminosity measured or inferred from the data, respectively, and $\mathcal{N}$ and $\mathcal{L}_X$ are used to indicate numbers and luminosities, respectively, that are predicted purely from the XRB scaling relations as described above.

3.3. Observed versus Predicted X-Ray Source Populations

We observe more X-ray sources above $S_{X,90}$ than predicted for the field of NGC 300 based on the ChaMP AGN log$N$-log$S$ distribution and the scaling relations of Lehmer et al. (2020, 2021). Figure 8 shows the observed radial source distribution (black), the AGN contribution inferred from the ChaMP log$N$-log$S$ distribution (red), the observed X-ray source population expected to be intrinsic to NGC 300 (blue), and the combined HMXB and LMXB population expected from the XRB scaling relations (dashed purple) above $S_{X,90}$. Only in the central region ($r \leqslant R_d$) of NGC 300 is there near-consistency between observations and predictions (owing to the large

Table 6
The Predicted and Inferred X-Ray Source Population in NGC 300

(1)	Galaxy Integrated ($r \leqslant 4R_d$) (2)	Radial Bin $r \leqslant R_d$ (3)	Radial Bin $R_d < r \leqslant 2R_d$ (4)	Radial Bin $2R_d < r \leqslant 3R_d$ (5)	Radial Bin $3R_d < r \leqslant 4R_d$ (6)	Sum of All Radial Bins (7)
($>S_{X,90}$)						
Observed X-Ray Point Sources						
N_X	70	6	16	22	26	⋯
N_{AGN}[a]	42.8 ± 2.1	2.8 ± 0.1	8.0 ± 0.4	14.1 ± 0.8	17.9 ± 0.9	⋯
$N_{AGN^{HR}}$[b]	52	3	13	16	20	⋯
N_{XRB}^{HR}[b]	18	3	3	6	6	⋯
N_{int} ($>L_{X,90}$)	27.2 ± 2.1	3.2 ± 0.1	8.0 ± 0.4	7.9 ± 0.8	8.1 ± 0.9	⋯
N_{int} ($>10^{37}$ erg s^{-1})	6.4 ± 0.4	0.6 ± 0.1	2.8 ± 0.1	3.0 ± 0.1	<0.2	⋯
$L^d_{X,\ int}$ (10^{38} erg s^{-1})	4.9 ± 0.4	0.16 ± 0.03	3.9 ± 0.3	0.4 ± 0.1	0.4 ± 0.2	⋯
Predicted X-Ray Point Sources[c]						
$\mathcal{N}_{HMXB}$ ($>L_{X,90}$)	4^{+2}_{-3}	1 ± 1	3^{+2}_{-1}	2^{+2}_{-1}	1 ± 1	7^{+6}_{-4}
$\mathcal{N}_{HMXB}$ ($>10^{37}$ erg s^{-1})	4^{+2}_{-1}	1 ± 1	2^{+2}_{-1}	2 ± 1	1 ± 1	6^{+5}_{-4}
$\mathcal{N}_{LMXB}$ ($>L_{X,90}$)	3 ± 2	1^{+2}_{-1}	2 ± 1	2^{+2}_{-1}	1 ± 1	6^{+6}_{-4}
$\mathcal{N}_{LMXB}$ ($>10^{37}$ erg s^{-1})	2^{+2}_{-1}	1 ± 1	1^{+2}_{-1}	1 ± 1	1 ± 1	4^{+5}_{-4}
$\mathcal{N}_{HMXB+LMXB}$ ($>L_{X,90}$)	7^{+4}_{-5}	2^{+3}_{-2}	5^{+3}_{-2}	4^{+4}_{-2}	2 ± 2	13^{+12}_{-8}
$\mathcal{L}_X$(HMXB) (10^{38} erg s^{-1})	$7.6^{+2.6}_{-2.2}$	0.6 ± 0.3	$4.3^{+1.3}_{-1.1}$	$2.6^{+1.2}_{-1.1}$	$0.6^{+0.3}_{-0.2}$	$8.1^{+3.1}_{-2.7}$
$\mathcal{L}_X$(LMXB) (10^{38} erg s^{-1})	$4.5^{+0.5}_{-0.4}$	1.0 ± 0.2	1.6 ± 0.2	0.7 ± 0.1	0.5 ± 0.1	3.8 ± 0.6
$\mathcal{L}_X^{HMXB+LMXB}$ (10^{38} erg s^{-1})	$12.1^{+3.1}_{-2.6}$	1.6 ± 0.5	$5.9^{+1.5}_{-1.3}$	$3.3^{+1.3}_{-1.2}$	$1.1^{+0.4}_{-0.3}$	$11.9^{+3.7}_{-3.3}$

Notes.
[a] Inferred from the AGN log$N$–log$S$ distribution (Kim et al. 2004).
[b] Number of AGN and XRB candidates inferred from hardness ratio analysis.
[c] Values are not corrected for the true L_X of NGC 300 ULX-1 (see Section 3.3 for details); when corrected for NGC 300 ULX-1, the galaxy-integrated $L_{X,\ int}$ is 4.43×10^{39} erg s^{-1}, and the corresponding radial bin ($R_d < r \leqslant 2R_d$) $L_{X,\ int}$ becomes 4.36×10^{39} erg s^{-1}. Subgalactic regions are modeled independently; the sums in columns (3)–(6) agree (within the uncertainties) with the spatially integrated results in column (2).

uncertainties in the expected number of XRBs), while the observed number of X-ray sources in the outer three regions exceeds predictions by $\gtrsim 3\sigma$.

The excess number of observed X-ray sources is also apparent in the XLF, as shown in Figure 9. The unabsorbed luminosity of an X-ray source is dependent on the spectral model assumed; oftentimes, a fiducial spectral model appropriate for both XRBs and AGN is assumed (usually an absorbed power law) and used to convert count rates to unabsorbed luminosities. We first use WebPIMMS[13] to implement this approach, assuming a power-law model with a photon index $\Gamma = 1.7$ that is subject to the Galactic absorbing column ($N_H = 10^{21}$ cm^{-2} toward NGC 300; HI4PI Collaboration et al. 2016) to convert the measured count rates to fluxes (and then into luminosities using the distance to NGC 300). The cumulative XLF can then be computed using

$$N(>S) = \sum_{i, S_i > S} \frac{1}{A(S_i)}, \quad (7)$$

where $A(S)$ is the area over which a source with flux S could be detected as measured from the sensitivity curves in Section 3.1. The resulting cumulative XLF is shown in black in Figure 9. There is one striking example of a source in NGC 300 where the assumption of a fiducial spectral model fails to yield a realistic luminosity approximation: NGC 300 ULX-1. Detailed observations of this source by XMM-Newton and NuSTAR indicate a relatively constant luminosity of $\sim 4 \times 10^{39}$ erg s^{-1},

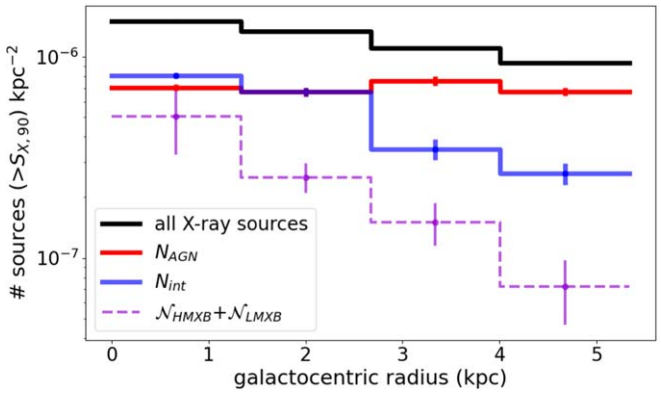

Figure 8. Radial distribution of all X-ray sources (black), the AGN contribution inferred from the ChaMP log$N$-log$S$ distribution (red), the observed X-ray source population expected to be intrinsic to NGC 300 (blue), and the combined HMXB and LMXB population expected from the XRB scaling relations (dashed purple).

with the modest count rates observed by Chandra likely the result of significant local obscuration by a precessing accretion disk (see, e.g., Binder et al. 2020, and references therein). We thus replace the fiducial model luminosity for NGC 300 ULX-1 with the "true" luminosity of the source, and recalculate a "corrected" XLF (dotted–dashed gray line in Figure 9). We additionally show the ChaMP AGN log$N$-log$S$ distribution (red Kim et al. 2004) and the synthetic HMXB (dashed blue) and LMXB (dotted–dashed dark red) XLFs described in the previous section. The total predicted XLF (AGN + HMXB + LMXB)

[13] https://heasarc.gsfc.nasa.gov/cgi-bin/Tools/w3pimms/w3pimms.pl

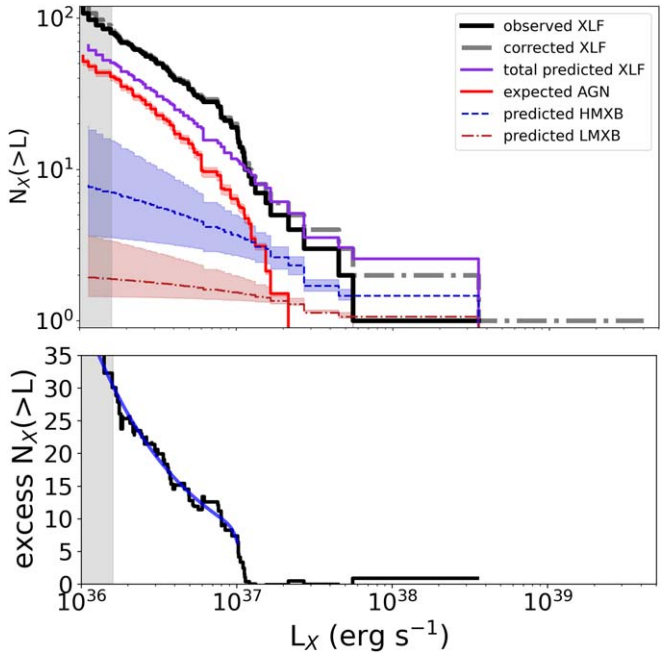

Figure 9. Top: The spatially integrated XLF of NGC 300. The solid black line shows the observed XLF when a fiducial spectral model is used to directly convert count rates to luminosities, while the dotted–dashed gray line shows the XLF after correcting for the "true" X-ray luminosity of NGC 300 ULX-1. The predicted contributions of AGN, HMXBs, and LMXBs are shown as solid red, dashed blue, and dotted–dashed dark red lines, respectively (the shaded region indicates uncertainties), and the sum of these three components is shown in purple. Bottom: The "excess" XLF (the difference between the gray and purple distributions in the top panel) with a broken power-law model (blue) superimposed. Only the horizontal axis uses a logarithmic scale, which makes the power-law model appear curved. The gray shaded region indicates the 90% limiting luminosity cutoff.

and the corresponding uncertainties are shown in purple. When we replace the incorrect inferred L_X of NGC 300 ULX-1 (from the fiducial model) with the more accurate L_X, we find that galaxy-integrated $L_{X,int}$ in Table 6 becomes $(4.43 \pm 0.04) \times 10^{39}$ erg s^{-1}. The value of $L_{X,int}$ becomes $(4.36 \pm 0.03) \times 10^{39}$ erg s^{-1} in the radial bin containing NGC 300 ULX-1 ($R_d < r \leqslant 2R_d$).

There is excellent agreement between the "corrected" observed XLF and the predicted XLF above $\sim 10^{37}$ erg s^{-1}. Below this value, we observe $\sim$20 more X-ray sources than predicted based on the survey area, stellar mass, and SFR. If we attempt to describe the low-flux end of the XLF by increasing the AGN contribution, the assumed survey area must be increased by $\sim$60%, which is well in excess of any area corrections derived from the uncertainties in R_d. Furthermore, increasing the AGN contribution leads to a clear excess of sources at $\sim(1-4) \times 10^{37}$ erg s^{-1}, where our survey is expected to be highly complete.

We subtract the observed XLF from the predicted XLF and show the resulting "excess" XLF in the bottom panel of Figure 9. Both a broken power-law model and an exponential cutoff model describe the shape of this excess XLF well; in either case, the faint-end slope is $\sim$0.7 with a break at $\sim 10^{37}$ erg s^{-1}. In the broken power-law model, the bright-end slope is very steep ($\gg$5) but largely unconstrained. There are two plausible explanations for the observed excess: (1) missing AGN, as the faint-end slope is broadly consistent with the faint end of the AGN log$N$-log$S$ distribution, and (2) variable sources, as the broken power-law shape of the excess XLF matches the predicted shape of the XLF of simulated variable XRBs (Binder et al. 2017). The XRB scaling relations from Equation (6) were derived from on-average brighter XRB populations (largely above 10^{37} erg s^{-1}) than those observed in the merged NGC 300 image, and as shown in Figure 9 (top panel), the uncertainties in the HMXB XLF at luminosities below 10^{37} erg s^{-1} are significant. If we assume that all of the excess sources below 10^{37} erg s^{-1} are XRBs, their total L_X would be $\sim 2.5 \times 10^{37}$ erg s^{-1}, which is comparable to the uncertainties on the predicted $\mathcal{L}_X$ values from the XRB scaling relations (see Table 6). Although the HMXB XLF (and corresponding L_X/SFR scaling relation) adequately predicts the integrated L_X of NGC 300, it does not predict the total number of objects in the galaxy below $\sim 10^{37}$ erg s^{-1}.

4. Discussion

Numerous works have investigated the relationship between the number and collective luminosity of HMXBs and host galaxy SFR and metallicity. However, the majority of these studies have utilized galaxy-integrated measurements of SFR and Z, and have largely targeted vigorously star-forming nearby galaxies to ensure a well-populated high-luminosity HMXB XLF. We now compare the results of our subgalactic analysis of NGC 300 to two key prior results: the N_{HMXB}–SFR relationship (Mineo et al. 2012) and the L_X–SFR–Z relationship. We seek to emphasize (1) that SFHs of more localized regions within a galaxy can vary, for example as a result of inside-out disk growth, which leads to measurable differences in the XRB populations that form; (2) that metallicity gradients provide a means to test metallicity dependence of observable XRB properties within a single galaxy; and (3) that HMXB–SFR scaling relations may not be reliable tools for predicting the XRB population below $\sim 10^{37}$ erg s^{-1}.

There is evidence that HMXBs, in particular, are related to even more local conditions than considered here: for example, Williams et al. (2013) used CMD fitting of the HST-resolved stellar populations in the very local ($\sim$50 pc) vicinity of HMXB candidates in NGC 300 and found that the SFRs of HMXB-hosting regions were a factor of $\sim$2.5 higher than that of randomly selected regions roughly $\sim$40–60 Myr ago. HMXB formation, however, is an intrinsically rare and stochastic process—not all highly localized regions that experienced a similar increase in SFR $\sim$50 Myr produce an HMXB—so additional assumptions about, e.g., the HMXB formation efficiency are required to compared these results to the galaxy-integrated literature. We additionally examine whether highly localized ($\sim$100 pc) environments around XRB candidates exhibit significant differences in SFH or metallicity than the subgalactic annular regions discussed above.

4.1. The N_{HMXB}–SFR Relationship

Since our observations are not able to definitively separate HMXBs from LMXBs for a majority of sources in NGC 300, we assume that the *relative* number and luminosities of HMXBs to LMXBs follow the predictions of the XRB scaling relations for each subgalactic bin to estimate the number of HMXBs (and the integrated L_X of these HMXBs) in each radial

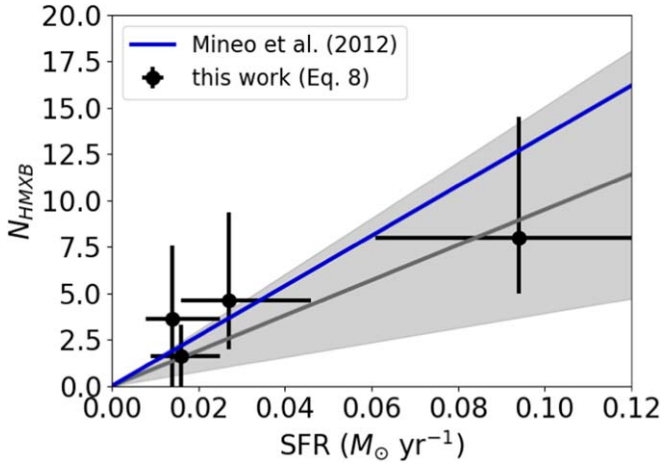

Figure 10. The number of HMXBs above $L_{X,90}$ (given by Equation (8)) as a function of SFR in NGC 300. Black points show our data; the best-fit linear relationship (and the 3σ uncertainty) is shown in gray. The solid blue line shows the relationship derived by Mineo et al. (2012).

bin. In other words,

$$N_{\rm HMXB} = N_{\rm int} \times \left(\frac{\mathcal{N}_{\rm HMXB}}{\mathcal{N}_{\rm HMXB} + \mathcal{N}_{\rm LMXB}}\right) \quad (8)$$

and

$$L_{\rm HMXB} = L_{\rm int} \times \left(\frac{\mathcal{L}_{\rm HMXB}}{\mathcal{L}_{\rm HMXB} + \mathcal{L}_{\rm LMXB}}\right). \quad (9)$$

Mineo et al. (2012) observed a linear relationship between the number of HMXBs observed in a galaxy and the host galaxy SFR. In that work, a single power-law XLF was fit to the bright ($>10^{37}$ erg s^{-1}) HMXB population and used to predict the total number of HMXBs above 10^{35} erg s^{-1}. To compare with those results, in Figure 10, we plot the predicted number of HMXBs above $L_{X,90}$ as a function of SFR for the four subgalactic regions within NGC 300. A simple linear regression fit yields

$$N_{\rm HMXB}(>10^{36}\ {\rm erg\ s^{-1}}) = (95 \pm 19)\left(\frac{\rm SFR}{M_\odot\ {\rm yr^{-1}}}\right). \quad (10)$$

The slope of this relationship is in good agreement (within $\sim 2\sigma$) with Mineo et al. (2012, slope of 135), which is remarkable given the very different populations of sources considered and different assumptions invoked in the two studies. Assuming the predicted number of HMXBs, $\mathcal{N}_{\rm HMXB}$, derived from the $L_{\rm X}$/SFR scaling relation yields a significantly shallower slope: 43 ± 5. We can additionally estimate the HMXB production rate by dividing the expected number of HMXBs in each subgalactic region by the total stellar mass formed in the last 100 Myr within each region. Across all four subgalactic regions within NGC 300, we estimate an HMXB production rate of $\sim(1\text{–}2)\times10^{-6}\ M_\odot^{-1}$. These values are lower than observed in M33 (Lazzarini et al. 2023), but are comparable to the production rates of HMXBs in M31 $\lesssim$50 Myr ago (Lazzarini et al. 2021). The agreement between expected number of HMXBs and the HMXB production rate to other dedicated HMXB studies suggests that the extra X-ray sources observed below 10^{37} erg s^{-1} are dominated by HMXBs, and not AGN.

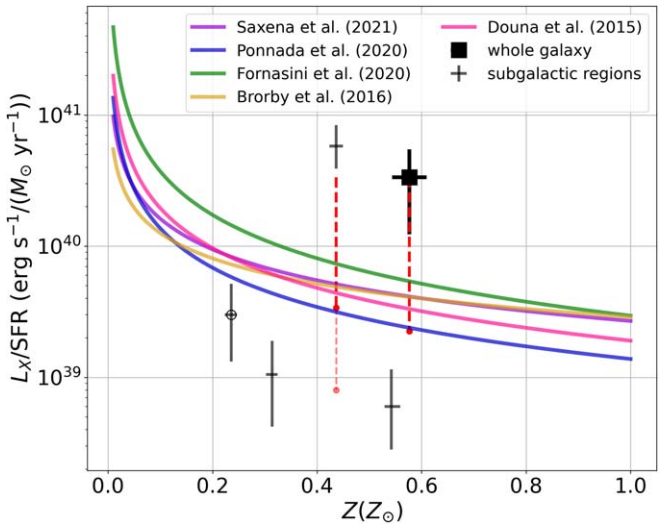

Figure 11. The ratio of $L_{\rm X}$/SFR as a function of metallicity for the four subgalactic regions in NGC 300 (gray) and the whole galaxy within $4R_{\rm d}$ (black) compared to recent $L_{\rm X}$–SFR–Z relationships from the literature. Uncertainties in the literature relationships are typically on the order of $\sim$0.5 dex. The point at $Z \approx 0.43Z_\odot$ indicates the subgalactic region containing the two brightest (and youngest) sources in NGC 300: NGC 300 X-1 and NGC 300 ULX-1. The vertical bright, dashed red lines show the effect of removing NGC 300 ULX-1 from our analysis, while the faint, dashed red line shows the effect of additionally removing NGC 300 X-1. The only subgalactic region with a constant SFR between 0–30 Myr and 30–100 Myr is indicated with an open circle.

4.2. The L_X–SFR–Z Relationship

In Figure 11, we compare our subgalactic (and galaxy-integrated) observations of NGC 300 to several $L_{\rm X}$–SFR–Z relationships from the literature (uncertainties in the literature relationships are typically on the order of $\sim$0.5 dex). To estimate the $L_{\rm X}$ originating from HMXBs only, we take the observed $L_{\rm X,\ int}$ from Table 6 and multiply it by the percentage of the predicted $\mathcal{L}_{\rm X}$ originating in HMXBs from the XRB scaling relations. The predicted $\mathcal{L}_{\rm X}$ was determined from simulating XRB populations from within the stellar mass and SFRs for NGC 300, so the uncertainties on $\mathcal{L}_{\rm X}$ are inclusive of both measurement uncertainties and additional uncertainties that result from stochastic formation of very bright sources (Section 3.2). These uncertainties are comparable to the stochastic uncertainties in $L_{\rm X}$/SFR reported by Lehmer et al. (2021). We find that the galaxy-integrated $L_{\rm X}$/SFR ratio of NGC 300 agrees with predictions for the value of Z we measure from our SED modeling if the corrected $L_{\rm X}$ of NGC 300 ULX-1 is not used; using the higher $L_{\rm X}$ for this one source puts the galaxy-integrated $L_{\rm X}$/SFR ratio $\sim 1\sigma$ above the literature relationships. Two of the four subgalactic regions fall below the literature $L_{\rm X}$–SFR–Z relationships, while the outermost region (at the lowest Z) is consistent (within $\sim 1\sigma$) with the literature relationships. The only radial bin that lies above the literature results is the bin from $R_d < r \leqslant 2R_d$, which has the highest recent SFR and contains the two youngest and brightest HMXBs in NGC 300: ULX-1 and X-1. If we exclude NGC 300 ULX-1 from our analysis, the predicted $\mathcal{L}_{\rm X}$ for HMXBs from the XRB scaling relations in Equation (6) is consistent with the observed $L_{\rm X}$ of NGC 300 X-1, and the $L_{\rm X}$/SFR ratio for this radial bin becomes consistent with literature $L_{\rm X}$–SFR–Z relationships (bright red, dashed line in Figure 11).

Figure 11 thus demonstrates the effect that stochastic formation of bright HMXBs in modestly star-forming galaxies can have on the observed L_X/SFR ratio. Many ULXs of comparable L_X to NGC 300 ULX-1 are located within galaxies with ongoing and significantly higher SFRs (often by an order of magnitude or more) than that observed in NGC 300, which is past the peak of its SFH. When NGC 300 ULX-1 is excluded, the subgalactic region at $R_d < r \leqslant 2R_d$ ($Z \approx 0.4Z_\odot$) is the only radial bin consistent with literature L_X–SFR–Z relationships (bright, dashed red line in Figure 11). The remaining L_X from this region is dominated by the Wolf–Rayet + BH binary NGC 300 X-1 (Binder et al. 2021), which is assumed to be extremely young based on the high masses of both the BH and donor star. The outermost radial bin ($Z \approx 0.25Z_\odot$) falls below the literature L_X–SFR–Z relationships only by $\sim 1\sigma - 2\sigma$. This is the only subgalactic region where the SFR increased (by $\sim$30%) in the last 30 Myr compared to 30–100 Myr ago, and so likely contains a higher proportion of younger, more massive HMXBs compared to other regions of NGC 300.

These differences in the L_X/SFR ratios of the subgalactic regions within NGC 300 may be hinting at an HMXB stellar age effect on the L_X–SFR–Z relationship, although, with a limited number of data points, it is difficult to draw any firm conclusions. That X-ray emission from XRB populations evolves as a function of time is not new (Fragos et al. 2013b; Antoniou et al. 2019; Lehmer et al. 2019), but this effect is difficult to directly measure on the short timescales over which HMXBs evolve ($\lesssim$100 Myr). The XLFs of LMXBs reveal that older galaxies tend to host a larger number of faint LMXBs ($\lesssim 10^{37}$ erg s^{-1}) compared to younger galaxies, and that the frequency of bright- and ULX-class LMXBs is much higher in younger galaxies (Zhang et al. 2012). The duration of the HMXB phase for a single binary is expected to be short ($\sim 10^4$ yr, Mineo et al. 2012). If more massive HMXBs are systematically more luminous than lower-mass HMXBs, one would expect the X-ray emission from an HMXB population to shift from younger/brighter systems to older/fainter systems over time, and in the absence of renewed star formation episodes, the collective L_X would diminish as brighter systems begin to "turn off." The evolution of $L_X/M_\star$ in star-forming galaxies over cosmic time has been examined both observationally (Gilbertson et al. 2022) and theoretically (Linden et al. 2010; Fragos et al. 2013a, 2013b), and this study of NGC 300, which approximately controls stellar age on timescales <100 Myr, provides another framework by which HMXB age evolution could be studied further.

Prior studies have systematically selected higher-SFR galaxies with ongoing star formation for analysis, which results in a proportionally larger population of young and luminous HMXBs (akin to NGC 300 ULX-1 and NGC 300 X-1) compared to the more "typical," moderate-luminosity $\sim$40–60 Myr HMXBs that are readily detectable in nearby galaxies (in NGC 300, but also the Magellanic Clouds, M31, M33, and NGC 2403; Antoniou et al. 2010; Williams et al. 2013; Antoniou & Zezas 2016; Lazzarini et al. 2021, 2023). We note that, if NGC 300 X-1 were to evolve out of its current X-ray bright phase, the L_X/SFR ratio of its corresponding subgalactic region would follow the general downward trend toward higher metallicities seen in the other three radial bins (faint red, dashed line in Figure 11). While the stochastic formation of very bright and short-lived HMXBs is expected to be influenced by metallicity, the current understanding of the L_X–SFR–Z relationship and XRB scaling relations is likely biased toward this small subset of younger, brighter HMXBs. Whether increasing stellar ages result in an L_X–SFR–Z relationship with a different normalization or slope (or both) compared to the one derived from presumably younger HMXBs is uncertain based on the present study; a more rigorous test of the effect of stellar age on the HMXB L_X–SFR–Z relationship would require a comprehensive study of the fainter HMXB populations in modestly star-forming galaxies with spatially resolved SFHs and metallicity gradients.

Evidence of variation and evolution in the L_X–SFR–Z relationship may be hidden within the significant scatter seen in previous studies. The literature L_X–SFR–Z relationships were derived using a variety of SFR indicators and stellar IMF assumptions, and some of the scatter in these relationships may originate from a heterogeneous mix of SFR tracers in addition to different assumptions about metallicity calibrations. Self-consistently modeling the modern SFRs, SFHs, and metallicities in subgalactic regions concurrently with the HMXBs population is required to firmly establish the extent to which stochastic and stellar age effects contribute to the L_X–SFR–Z relationship, and ultimately our understanding of massive binary star evolution.

4.3. Comparison to XRB-hosting Local Regions

The short lifetimes of HMXBs ($\lesssim$100 Myr) and relatively low natal kick velocities they experience during initial compact object formation (Giacobbo & Mapelli 2020) prevent HMXBs from traveling more than $\sim$100–200 pc from their birthplaces. We thus explored whether the environments directly associated with XRB candidate sources showed any significant differences in terms of their SFHs or metallicities compared to the larger annular regions described above.

We identified XRB candidate X-ray sources by excluding highly absorbed sources (e.g., those with HR1 $\geqslant$0.4, which are likely background AGN) and extracted photometry from circular apertures centered on the X-ray sources with radii of 10.3″ ($\sim$100 pc). We verified that none of the individual circular apertures overlapped; thus, the total area covered is 0.03 kpc × the number of XRB candidates in each annular region (from innermost to outermost region, we identify 4, 11, 7, and 10 XRB candidates). The SED resulting from the combined photometry from all XRB candidates within a given annular region is then modeled with PROSPECTOR in a manner identical to that described in Section 2.

The resulting SFHs and the metallicity gradients from both the XRB-hosting local regions and the larger annular regions are shown in Figure 12. To account for the significant differences in areas covered, we show the SFR surface density Σ_{SFR}. The SFHs of the XRB-hosting local regions generally show an enhancement in Σ_{SFR} the most recent (<30 Myr) time bin by factors of $\sim$3–10 while the SFRs observed in the 30–100 Myr time bins are consistent (within the large uncertainties) with those found from the annular analysis presented. This leads to an overall increase in the inferred SFR within the last 100 Myr in the locally derived SFR compared to the annuli-averaged SFR. The metallicity gradient derived from the XRB-hosting regions is nearly identical to the one derived from the larger annular regions. If the SFRs associated with XRBs is indeed higher than the annuli-averaged value, the L_X/SFR ratios shown on Figure 11 would be shifted down. The deviation between the NGC 300 subgalactic analysis and the literature L_X–SFR–Z relationships becomes more pronounced;

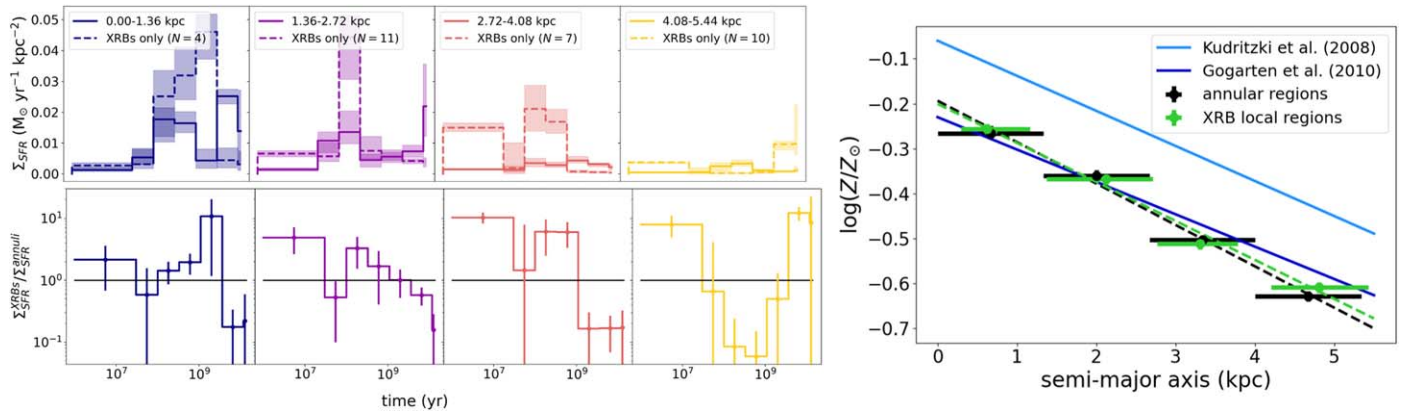

Figure 12. Left: The radially resolved SFHs of the annular regions (solid lines) compared to the stacked localized regions around XRB candidates (dashed lines; the number of XRB candidates used to derive the SFHs is indicated in the legend). Colors are as in Figure 6. Right: the metallicity gradient derived from the stacked localized regions containing XRBs (green) compared to the annular regions (black), Kudritzki et al. (2008, light blue), and Gogarten et al. (2010, dark blue).

the NGC 300 sources are underluminous for their metallicity and SFR. This is consistent with the finding in Section 3.3 (see also Figure 9), where we find evidence for an excess of possibly variable, low-luminosity XRB population in excess of the predictions from HMXB and LMXB scaling relations.

5. Summary

We have conducted a panchromatic analysis of the nearby galaxy NGC 300 on subgalactic scales to illustrate how spatially resolved studies of nearby galaxies can provide useful insights into the XRB–host galaxy connection. The 3.6 μm scale length (R_d) is used to divide the galaxy into four equal-width annular regions, and we perform aperture photometry to measure the UV-optical-IR flux densities within each subgalactic region. We then construct SEDs and use PROSPECTOR to measure the SFHs and present-day stellar masses, metallicities, and recent (<100 Myr) SFRs across the star-forming disk. The current galaxy-integrated stellar mass is $M_\star = (2.15^{+0.26}_{-0.14}) \times 10^9\ M_\odot$, and the current SFR is $\sim 0.18 \pm 0.07\ M_\odot\ \mathrm{yr}^{-1}$, in agreement with previous measurements. Our measured metallicity gradient and radially resolved SFH are also consistent with other gradients reported in the literature.

We used four archival Chandra observations to identify 70 X-ray sources within $4R_d$ that were detected at high significance. We used the ChaMP AGN log$N$-log$S$ distribution (Kim et al. 2004) and the XRB scaling relations of Lehmer et al. (2020, 2021) to compare the observed X-ray point-source population to the predicted X-ray point-source population. On a galaxy-integrated scale, the radial source distribution and XLF show a clear excess in the number of observed X-ray sources at luminosities $<10^{37}$ erg s^{-1}. The X-ray source excess is consistent with a faint and variable XRB population that is not well described by the assumed XRB scaling relations, with the possibility of additional AGN contamination. Our subgalactic analysis reveals the linear relationship between the number of HMXBs formed and SFR that is consistent with prior expectations that derived from a large, galaxy-integrated sample of more vigorously star-forming galaxies.

Most intriguingly, we find that the L_X/SFR ratios as a function of Z across the four subgalactic regions are only consistent with L_X–SFR–Z relationships from the literature for the bins that are likely to host the youngest HMXBs. These results hint at a possible trend in the L_X–SFR–Z relationship with stellar age, as lower-mass HMXBs begin to dominate the total L_X of a galaxy after the star formation episode that formed those systems ends. We derive SFHs for the local (∼100 pc) regions immediately surrounding XRB candidate sources and find that their recent (<30 Myr) SFR surface densities are generally higher than those of the integrated annular regions, which decreases the L_X/SFR ratio and makes the underluminous nature of the NGC 300 XRB population even more pronounced. Expanding this analysis to a larger sample of nearby galaxies that are just past their peak of star formation, and where the fainter X-ray source population can be studied on subgalactic scales (and the spatially resolved SFH can be directly modeled), is needed to further investigate possible trends in the L_X/SFR ratio with both metallicity and stellar age.

Acknowledgments

B.A.B. acknowledges support from the National Science Foundation Launching Early-Career Academic Pathways in the Mathematical and Physical Sciences (LEAPS-MPS) award No. 2213230. This paper employs a list of Chandra data sets, obtained by the Chandra X-ray Observatory, contained in DOI:10.25574/cdc.204, and software provided by the Chandra X-ray Center (CXC) in the application package CIAO. This research made use of Astropy, a community-developed core Python package for Astronomy (Astropy Collaboration et al. 2013, 2018, 2022).

Facilities: Chandra X-ray Observatory, Swift (UVOT), GALEX, CTIO:2MASS, FLWO:2MASS , Spitzer (IRAC and MIPS), WISE.

Software: astropy (Astropy Collaboration et al. 2013, 2018, 2022), CIAO (Fruscione et al. 2006).

ORCID iDs

Breanna A. Binder https://orcid.org/0000-0002-4955-0471
Michael Eracleous https://orcid.org/0000-0002-3719-940X
Alexander Belles https://orcid.org/0000-0002-8606-0797
Benjamin F. Williams https://orcid.org/0000-0002-7502-0597

References

Antoniou, V., & Zezas, A. 2016, MNRAS, 459, 528
Antoniou, V., Zezas, A., Drake, J. J., et al. 2019, ApJ, 887, 20
Antoniou, V., Zezas, A., Hatzidimitriou, D., & Kalogera, V. 2010, ApJL, 716, L140

Asplund, M., Grevesse, N., Sauval, A. J., & Scott, P. 2009, ARA&A, 47, 481
Astropy Collaboration, Price-Whelan, A. M., Lim, P. L., et al. 2022, ApJ, 935, 167
Astropy Collaboration, Price-Whelan, A. M., Sipőcz, B. M., et al. 2018, AJ, 156, 123
Astropy Collaboration, Robitaille, T. P., Tollerud, E. J., et al. 2013, A&A, 558, A33
Basu-Zych, A. R., Lehmer, B., Fragos, T., et al. 2016, ApJ, 818, 140
Basu-Zych, A. R., Lehmer, B. D., Hornschemeier, A. E., et al. 2013, ApJ, 774, 152
Belfiore, F., Vincenzo, F., Maiolino, R., & Matteucci, F. 2019, MNRAS, 487, 456
Belles, A., Decleir, M., Bowman, W. P., et al. 2023, ApJ, 953, 54
Berg, D. A., Skillman, E. D., Croxall, K. V., et al. 2015, ApJ, 806, 16
Binder, B., Gross, J., Williams, B. F., et al. 2017, ApJ, 834, 128
Binder, B., Williams, B. F., Eracleous, M., et al. 2012, ApJ, 758, 15
Binder, B. A., Anderson, A. K., Garofali, K., Lazzarini, M., & Williams, B. F. 2023, MNRAS, 522, 5669
Binder, B. A., Carpano, S., Heida, M., & Lau, R. 2020, Galax, 8, 17
Binder, B. A., Sy, J. M., Eracleous, M., et al. 2021, ApJ, 910, 74
Bodaghee, A., Tomsick, J. A., Rodriguez, J., & James, J. B. 2012, ApJ, 744, 108
Boroson, B., Kim, D.-W., & Fabbiano, G. 2011, ApJ, 729, 12
Breeveld, A. A., Curran, P. A., Hoversten, E. A., et al. 2010, MNRAS, 406, 1687
Breeveld, A. A., Landsman, W., Holland, S. T., et al. 2011, in AIP Conf. Ser. 1358, Gamma Ray Bursts 2010, ed. J. E. McEnery, J. L. Racusin, & N. Gehrels (Melville, NY: AIP), 373
Bresolin, F., Gieren, W., Kudritzki, R.-P., et al. 2009, ApJ, 700, 309
Brorby, M., Kaaret, P., Prestwich, A., & Mirabel, I. F. 2016, MNRAS, 457, 4081
Brorby, M., Kaaret, P., & Prestwich, A. 2014, MNRAS, 441, 2346
Clauset, A., Shalizi, C. R., & Newman, M. E. J. 2009, SIAMR, 51, 661
Colbert, E. J. M., Heckman, T. M., Ptak, A. F., Strickland, D. K., & Weaver, K. A. 2004, ApJ, 602, 231
Croxall, K. V., Pogge, R. W., Berg, D. A., Skillman, E. D., & Moustakas, J. 2015, ApJ, 808, 42
Croxall, K. V., Pogge, R. W., Berg, D. A., Skillman, E. D., & Moustakas, J. 2016, ApJ, 830, 4
Cutri, R. M., Wright, E. L., Conrow, T., et al. 2013, in Explanatory Supplement to the AllWISE Data Release Products, ed. R. M. Cutri et al.
Dalcanton, J. J., Williams, B. F., Seth, A. C., et al. 2009, ApJS, 183, 67
de Vaucouleurs, G., de Vaucouleurs, A., Corwin, H. G. J., et al. 1991, Third Reference Catalogue of Bright Galaxies (New York: Springer)
Decleir, M., De Looze, I., Boquien, M., et al. 2019, MNRAS, 486, 743
Deharveng, L., Caplan, J., Lequeux, J., et al. 1988, A&AS, 73, 407
Douna, V. M., Pellizza, L. J., Mirabel, I. F., & Pedrosa, S. E. 2015, A&A, 579, A44
Fitzpatrick, E. L. 1999, PASP, 111, 63
Florido, E., Zurita, A., & Pérez-Montero, E. 2022, MNRAS, 513, 2006
Foreman-Mackey, D., Hogg, D. W., Lang, D., & Goodman, J. 2013, PASP, 125, 306
Fragos, T., Kalogera, V., Belczynski, K., et al. 2008, ApJ, 683, 346
Fragos, T., Lehmer, B., Tremmel, M., et al. 2013b, ApJ, 764, 41
Fragos, T., Lehmer, B. D., Naoz, S., Zezas, A., & Basu-Zych, A. 2013a, ApJL, 776, L31
Fruscione, A., McDowell, J. C., Allen, G. E., et al. 2006, Proc. SPIE, 6270, 62701V
Gaia Collaboration, Vallenari, A., Brown, A. G. A., et al. 2023, A&A, 674, A1
Gehrels, N., Chincarini, G., Giommi, P., et al. 2004, ApJ, 611, 1005
Georgakakis, A., Nandra, K., Laird, E. S., Aird, J., & Trichas, M. 2008, MNRAS, 388, 1205
Giacobbo, N., & Mapelli, M. 2020, ApJ, 891, 141
Gil de Paz, A., Boissier, S., Madore, B. F., et al. 2007, ApJS, 173, 185
Gilbertson, W., Lehmer, B. D., Doore, K., et al. 2022, ApJ, 926, 28
Gilfanov, M. 2004, MNRAS, 349, 146
Gilfanov, M., Grimm, H. J., & Sunyaev, R. 2004, MNRAS, 347, L57
Gogarten, S. M., Dalcanton, J. J., Williams, B. F., et al. 2010, ApJ, 712, 858
Goodman, J., & Weare, J. 2010, CAMCS, 5, 65
Greco, J. P., Goulding, A. D., Greene, J. E., et al. 2018, ApJ, 866, 112
Grimm, H. J., Gilfanov, M., & Sunyaev, R. 2003, MNRAS, 339, 793
Gross, J., Williams, B. F., Pannuti, T. G., et al. 2019, ApJ, 877, 15
Helou, G., Roussel, H., Appleton, P., et al. 2004, ApJS, 154, 253
HI4PI Collaboration, Ben Bekhti, N., Flöer, L., et al. 2016, A&A, 594, A116
Jang, I. S., de Jong, R. S., Minchev, I., et al. 2020, A&A, 640, L19
Jarrett, T. H., Chester, T., Cutri, R., Schneider, S. E., & Huchra, J. P. 2003, AJ, 125, 525
Johnson, B. D., Leja, J., Conroy, C., & Speagle, J. S. 2021, ApJS, 254, 22
Kaisina, E. I., Makarov, D. I., Karachentsev, I. D., & Kaisin, S. S. 2012, AstBu, 67, 115
Karachentsev, I. D., & Kaisina, E. I. 2013, AJ, 146, 46
Kaur, H. D., Qin, Y., Mesinger, A., et al. 2022, MNRAS, 513, 5097
Kewley, L. J., & Dopita, M. A. 2002, ApJS, 142, 35
Kewley, L. J., & Ellison, S. L. 2008, ApJ, 681, 1183
Kim, D.-W., & Fabbiano, G. 2010, ApJ, 721, 1523
Kim, D. W., Wilkes, B. J., Green, P. J., et al. 2004, ApJ, 600, 59
Kouroumpatzakis, K., Zezas, A., Sell, P., et al. 2020, MNRAS, 494, 5967
Kreckel, K., Ho, I. T., Blanc, G. A., et al. 2020, MNRAS, 499, 193
Kroupa, P. 2001, MNRAS, 322, 231
Kudritzki, R.-P., Urbaneja, M. A., Bresolin, F., et al. 2008, ApJ, 681, 269
Laine, J., Laurikainen, E., & Salo, H. 2016, A&A, 596, A25
Laird, E. S., Nandra, K., Georgakakis, A., et al. 2009, ApJS, 180, 102
Lazzarini, M., Hinton, K., Shariat, C., et al. 2023, ApJ, 952, 114
Lazzarini, M., Williams, B. F., Durbin, M., et al. 2021, ApJ, 906, 120
Lee, J. C., Gil de Paz, A., Tremonti, C., et al. 2009, ApJ, 706, 599
Lehmer, B. D., Alexander, D. M., Bauer, F. E., et al. 2010, ApJ, 724, 559
Lehmer, B. D., Berkeley, M., Zezas, A., et al. 2014, ApJ, 789, 52
Lehmer, B. D., Eufrasio, R. T., Basu-Zych, A., et al. 2021, ApJ, 907, 17
Lehmer, B. D., Eufrasio, R. T., Tzanavaris, P., et al. 2019, ApJS, 243, 3
Lehmer, B. D., Ferrell, A. P., Doore, K., et al. 2020, ApJS, 248, 31
Leja, J., Carnall, A. C., Johnson, B. D., Conroy, C., & Speagle, J. S. 2019, ApJ, 876, 3
Leja, J., Johnson, B. D., Conroy, C., van Dokkum, P. G., & Byler, N. 2017, ApJ, 837, 170
Leja, J., Johnson, B. D., Conroy, C., & van Dokkum, P. 2018, ApJ, 854, 62
Liang, Y. C., Hammer, F., & Yin, S. Y. 2007, A&A, 474, 807
Linden, T., Kalogera, V., Sepinsky, J. F., et al. 2010, ApJ, 725, 1984
Martin, D. C., Fanson, J., Schiminovich, D., et al. 2005, ApJL, 619, L1
Martín-Hernández, N. L., Peeters, E., Morisset, C., et al. 2002, A&A, 381, 606
McGaugh, S. S. 1991, ApJ, 380, 140
Micheva, G., Roth, M. M., Weilbacher, P. M., et al. 2022, A&A, 668, A74
Mineo, S., Gilfanov, M., & Sunyaev, R. 2012, MNRAS, 419, 2095
Mondal, C., Subramaniam, A., & George, K. 2019, JApA, 40, 35
Morrissey, P., Conrow, T., Barlow, T. A., et al. 2007, ApJS, 173, 682
Ocvirk, P., Pichon, C., Lançon, A., & Thiébaut, E. 2006, MNRAS, 365, 46
Oyarzún, G. A., Bundy, K., Westfall, K. B., et al. 2019, ApJ, 880, 111
Pandya, V., Romanowsky, A. J., Laine, S., et al. 2018, ApJ, 858, 29
Park, T., Kashyap, V. L., Siemiginowska, A., et al. 2006, ApJ, 652, 610
Patrício, V., Richard, J., Carton, D., et al. 2018, MNRAS, 477, 18
Pettini, M., & Pagel, B. E. J. 2004, MNRAS, 348, L59
Pilyugin, L. S., & Thuan, T. X. 2005, ApJ, 631, 231
Puche, D., Carignan, C., & Bosma, A. 1990, AJ, 100, 1468
Querejeta, M., Meidt, S. E., Schinnerer, E., et al. 2015, ApJS, 219, 5
Ranalli, P., Comastri, A., & Setti, G. 2003, A&A, 399, 39
Rieke, G. H., Young, E. T., Engelbracht, C. W., et al. 2004, ApJS, 154, 25
Roming, P. W. A., Kennedy, T. E., Mason, K. O., et al. 2005, SSRv, 120, 95
Rudolph, A. L., Fich, M., Bell, G. R., et al. 2006, ApJS, 162, 346
Salpeter, E. E. 1955, ApJ, 121, 161
Schlafly, E. F., & Finkbeiner, D. P. 2011, ApJ, 737, 103
Sheth, K., Regan, M., Hinz, J. L., et al. 2010, PASP, 122, 1397
Tremonti, C. A., Heckman, T. M., Kauffmann, G., et al. 2004, ApJ, 613, 898
Tzanavaris, P., Hornschemeier, A. E., Gallagher, S. C., et al. 2016, ApJ, 817, 95
Williams, B. F., Binder, B. A., Dalcanton, J. J., Eracleous, M., & Dolphin, A. 2013, ApJ, 772, 12
Williams, T. G., Kreckel, K., Belfiore, F., et al. 2022, MNRAS, 509, 1303
Wright, E. L., Eisenhardt, P. R. M., Mainzer, A. K., et al. 2010, AJ, 140, 1868
Zaritsky, D., Kennicutt, R. C. J., & Huchra, J. P. 1994, ApJ, 420, 87
Zhang, Z., Gilfanov, M., & Bogdán, Á. 2012, A&A, 546, A36
Zuo, Z.-Y., Li, X.-D., & Gu, Q.-S. 2014, MNRAS, 437, 1187